

AD-A135 897

EFFECT OF SUCTION ON THE WAKE STRUCTURE OF A
THREE-DIMENSIONAL TURRET(U) DAYTON UNIV OH RESEARCH
INST S C PUROHIT OCT 83 UDR-TR-83-64 AFWAL-TR-83-3099

1/1

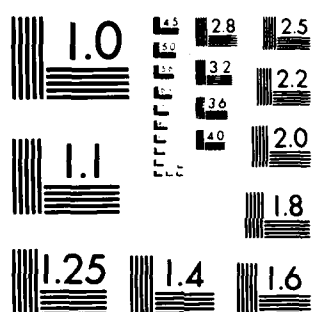
UNCLASSIFIED

F33615-82-K-3021

F/G 20/4

NL

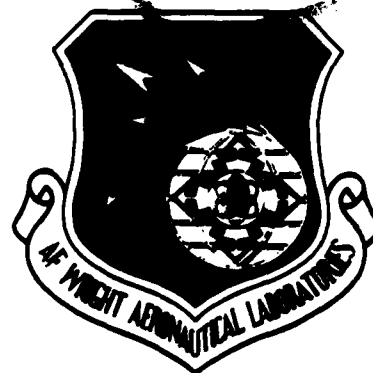
END
DATE
FILMED
11-84
DTIC



MICROCOPY RESOLUTION TEST CHART
NATIONAL BUREAU OF STANDARDS 1963-A

AFWAL-TR-83-3099

EFFECT OF SUCTION ON THE WAKE STRUCTURE
OF A THREE-DIMENSIONAL TURRET



S. C. PUROHIT
AEROSPACE MECHANICS DIVISION
UNIVERSITY OF DAYTON RESEARCH INSTITUTE
300 COLLEGE PARK
DAYTON, OHIO 45469

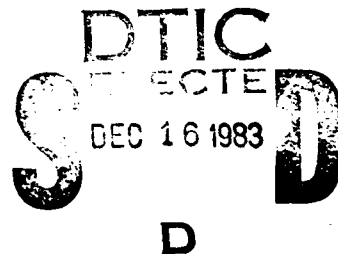
OCTOBER 1983

FINAL REPORT FOR PERIOD 1 DECEMBER 1982 - 17 AUGUST 1983

APPROVED FOR PUBLIC RELEASE; DISTRIBUTION UNLIMITED.

PREPARED FOR

FLIGHT DYNAMICS LABORATORY
AIR FORCE WRIGHT AERONAUTICAL LABORATORIES
AIR FORCE SYSTEMS COMMAND
WRIGHT-PATTERSON AIR FORCE BASE, OHIO 45433



DTIC FILE COPY


83 12 16 068

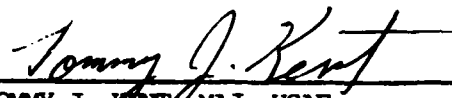
NOTICE

When Government drawings, specifications, or other data are used for any purpose other than in connection with a definitely related Government procurement operation, the United States Government thereby incurs no responsibility nor any obligation whatsoever; and the fact that the government may have formulated, furnished, or in any way supplied the said drawings, specifications, or other data, is not to be regarded by implication or otherwise as in any manner licensing the holder or any other person or corporation, or conveying any rights or permission to manufacture use, or sell any patented invention that may in any way be related thereto.

This report has been reviewed by the Office of Public Affairs (ASD/PA) and is releasable to the National Technical Information Service (NTIS). At NTIS, it will be available to the general public, including foreign nations.

This technical report has been reviewed and is approved for publication.


JOSEPH SHANG
Project Engineer
Aerodynamics & Airframe Branch
Aeromechanics Division


TOMMY J. KENT, MAJ, USAF
Chief, Aerodynamics & Airframe Branch
Aeromechanics Division

FOR THE COMMANDER


RALPH W. HOLM
Colonel, USAF
Chief, Aeromechanics Division

"If your address has changed, if you wish to be removed from our mailing list, or if the addressee is no longer employed by your organization please notify AEWAL/ETMA N-PAFB, OH 45433 to help us maintain a current mailing list".

Copies of this report should not be returned unless return is required by security considerations, contractual obligations, or notice on a specific document.

Unclassified

SECURITY CLASSIFICATION OF THIS PAGE (When Data Entered)

REPORT DOCUMENTATION PAGE		READ INSTRUCTIONS BEFORE COMPLETING FORM
1. REPORT NUMBER AFWAL-TR-83-3099	2. GOVT ACCESSION NO.	3. RECIPIENT'S CATALOG NUMBER
4. TITLE (and Subtitle) EFFECT OF SUCTION ON THE WAKE STRUCTURE OF A THREE-DIMENSIONAL TURRET		5. TYPE OF REPORT & PERIOD COVERED Final, 1 December 1982 - 17 August 1983
		6. PERFORMING ORG. REPORT NUMBER UDR-TR-83-64
7. AUTHOR(s) S. C. Purohit		8. CONTRACT OR GRANT NUMBER(s) F33615-82-K-3021
9. PERFORMING ORGANIZATION NAME AND ADDRESS University of Dayton Research Institute 300 College Park Avenue Dayton, Ohio 45469		10. PROGRAM ELEMENT, PROJECT, TASK AREA & WORK UNIT NUMBERS AIZ - JON: 2307N607 - CCC: 616100
11. CONTROLLING OFFICE NAME AND ADDRESS Flight Dynamics Laboratory (AFWAL/FIMM) AF Wright Aeronautical Laboratories (AFSC) Wright-Patterson AFB, Ohio 45433		12. REPORT DATE October 1983
		13. NUMBER OF PAGES 84
14. MONITORING AGENCY NAME & ADDRESS (if different from Controlling Office)		15. SECURITY CLASS. (of this report) Unclassified
		15a. DECLASSIFICATION/DOWNGRADING SCHEDULE
16. DISTRIBUTION STATEMENT (of this Report) Approved for public release; distribution unlimited.		
17. DISTRIBUTION STATEMENT (of the abstract entered in Block 20, if different from Report)		
18. SUPPLEMENTARY NOTES		
19. KEY WORDS (Continue on reverse side if necessary and identify by block number) Flowfield over a turret; unsteady three-dimensional flow; com- pressible Navier-Stokes equations; turbulent flow; vorticity, separated flow; wake structure; boundary layer suction		
20. ABSTRACT (Continue on reverse side if necessary and identify by block number) This report examines the flowfield over a three-dimensional turret when suction is applied to alter the wake structures. At a uniform rate of 0.136 kg/s, the numerical simulation of flow around a turret is accomplished through the solution of mass averaged unsteady compressible Navier-Stokes equations. The computation is performed, for a free stream Mach number 0.6 and Reynolds number $12.8 \times 10^6/m$, on the CRAY-1 computer utilizing		

DD FORM 1 JAN 73 1473 EDITION OF 1 NOV 65 IS OBSOLETE

Unclassified

SECURITY CLASSIFICATION OF THIS PAGE (When Data Entered)

Unclassified

SECURITY CLASSIFICATION OF THIS PAGE(When Data Entered)

20. 62 x 30 x 30 grid points. Using MacCormack's explicit finite difference scheme, the steady-state periodic solutions are achieved for the two cases when the turret is treated like a solid shell and a porous shell. The results are compared with available experimental data or known solution, and the numerical values for RMS density fluctuations and correlation coefficients are presented.



Succession For	
NTIS GRA&I	<input checked="" type="checkbox"/>
DTIC TAB	<input type="checkbox"/>
Unannounced	<input type="checkbox"/>
Justification	
By	
Distribution/	
Availability Codes	
Dist	Avail and/or Special
A/1	

Unclassified

SECURITY CLASSIFICATION OF THIS PAGE(When Data Entered)

PREFACE

This report covers the activities of Dr. Sharad C. Purohit in the area of Computational Fluid Dynamics while working as Visiting Scientist, Aerospace Mechanics Division, University of Dayton Research Institute, Dayton, Ohio. The work was funded by the Air Force Wright Aeronautical Laboratories/Flight Dynamics Laboratory, through Project No. 2307, Task No. N6, Work Unit 07, Contract No. F33615-82-K-3021 entitled, "Unsteady Flow About an Aircraft Turret."

The author acknowledges the support provided by Lt. Col. J. J. Russell and Capt. J. D. Waskiewicz of the Air Force Weapons Laboratory at Kirtland Air Force Base for the use of the CRAY-1 computer. The author is also indebted to Dr. W. L. Hankey, Jr. and Dr. J. S. Shang of the Flight Dynamics Laboratory, Air Force Wright Aeronautical Laboratories, Wright-Patterson Air Force Base for their valuable advice and stimulating discussion.

The opportunity extended to the author by the University of Dayton Research Institute, through the Visiting Scientist Program, has been technically rewarding. In particular, the support of Mr. Dale H. Whitford and Dr. James N. Scott of the Aerospace Mechanics Division is duly acknowledged.

This work was performed during the author's study leave from the Aeronautic Group, Vikram Sarabhai Space Centre, Indian Space Research Organisation, Trivandrum, India. The encouragement to conduct research by the Government of India is gratefully acknowledged.

TABLE OF CONTENTS

SECTION		PAGE
1	INTRODUCTION	1
2	GOVERNING EQUATIONS	3
3	TURBULENCE MODEL	15
4	NUMERICAL PROCEDURE	19
5	RESULTS AND DISCUSSION	23
6	CONCLUSIONS	67
	APPENDIX - VORTICITY FUNCTION	69
	REFERENCES	71

LIST OF ILLUSTRATIONS

FIGURE		PAGE
1	The Turret	7
2	Mesh System of the Turret	9
3	The Mesh Point Distribution on the Flat Surface	10
4	Boundary Conditions	13
5	Scale Lengths for the Turbulence Model	16
6	The Function TF Along 120° AZA	24
7	The Function TF Along 180° AZA	25
8	The Function TF Along 240° AZA	26
9	The Coefficient TF_{\max} for Various Time Levels	27
10	The Eddy Viscosity Coefficient	28
11	Typical Mesh Point Location	30
12	Pressure Coefficient at $\frac{Y}{R} = 1.2394$, (C_2)	31
13	Pressure Coefficient at $\frac{Y}{R} = 1.2394$, (D_2)	32
14	Pressure Coefficient at $\frac{Y}{R} = 1.627 \times 10^{-2}$, (B_1)	33
15	Comparison of Pressure Distribution for Flow Without Suction	34
16	Comparison of Pressure Distribution for Flow with Suction	35
17	Local Mach Number Variation at Mesh Point A_2	37
18	Local Mach Number Variation at Mesh Point B_2	38
19	Local Mach Number Variation at Mesh Point C_2	39
20	Instantaneous Velocity Field for Flow Without Suction in the Turret Shoulder Plane	40
21	The Typical Mesh Points for Body-Oriented and Cartesian Coordinate System	41
22	Wake Profiles for Flow Without Suction in the Turret Shoulder Plane	43

LIST OF ILLUSTRATIONS (Continued)

FIGURE		PAGE
23	Planar Plot of the Mach Number Distribution for Flow Without Suction in the Turret Shoulder Plane	44
24	Instantaneous Velocity Field Flow with Suction in the Turret Shoulder Plane	45
25	Wake Profiles for Flow with Suction in the Turret Shoulder Plane	46
26	Planar Plot of the Mach Number Distribution for Flow with Suction in the Turret Shoulder Plane	47
27	Velocity Field in the Cross-sectional Plane for the Flow Without Suction	48
28	Mach Number Distribution Close to the Turret Surface for the Flow Without Suction (a) On the Cylinder (b) On the Hemisphere	50
29	Velocity Field in the Cross-sectional Plane for the Flow with Suction	51
30	Mach Number Distribution Close to the Turret Surface for the Flow with Suction (a) On the Cylinder (b) On the Hemisphere	52
31	Instantaneous Limiting Streamline Pattern on the Flat Surface for the Flow Without Suction	53
32	Instantaneous Limiting Streamline Pattern on the Flat Surface for the Flow with Suction	54
33	Instantaneous Limiting Streamline Pattern on the Turret Surface for Flow Without Suction	55
34	Instantaneous Limiting Streamline Pattern on the Turret Surface for Flow with Suction	56
35	Mean Density Along 120° A2A	58
36	Comparison of RMS Density Fluctuations with Experimental Data	59

LIST OF ILLUSTRATIONS (Concluded)

FIGURE		PAGE
37	Correlation Coefficient for Flow Without Suction	61
38	Correlation Coefficient for Flow with Suction	62
39	Spectral Analysis Along 120° AZA	64
40	Phase Angle Analysis Along 120° AZA (a) Without Suction (b) With Suction	65

NOMENCLATURE

AZA	azimuth angle around the turret
CP	pressure coefficient
D	turret diameter
e	specific energy
e_i	specific internal energy
F,G,H	vector fluxes in mean flow equations
i,j,k	indices for grid point location
J	Jacobian of coordinate transformation
L	scale length
L^*	difference operator
MPA	meridian plane angle
P	pressure
Pr	molecular Prandtl number, 0.72
Pr_t	turbulent Prandtl number, 0.90
R	turret radius
R_{mn}	correlation coefficients for grid points j_m and j_n
t	time
TCH	characteristic time, D/U_∞
u,v,w	velocity component in Cartesian coordinates
U	mass averaged dependent variable
x,y,z	Cartesian coordinates
ρ	density
ξ,η,ζ	transformed coordinates
ϵ	eddy viscosity
ν	ratio of specific heats
μ	molecular viscosity coefficient
ω	vorticity
$\sigma_x, \sigma_y, \sigma_z$	normal stresses
$\tau_{xy}, \tau_{yz}, \tau_{zx}$	shear stresses

Subscripts

∞	free stream conditions
W	surface condition

Subscripts (Concluded)

FL	flat plate surface condition
T	turret surface condition
max	maximum value
min	minimum value

SECTION 1

INTRODUCTION

The assessment of unsteady flow structure around an airborne turret is of current interest in the aero-optical research area^{1,2}. The reduction of cumulative total system optical error is becoming increasingly important for design purposes. The major contributor to such degradation is the fluid mechanical interference. In particular, the complex turbulent mixing, entrainment process and the separated flow result in free shear layer oscillations. Although a complete physical understanding of this fluid dynamics is lacking, significant progress has been made in the past few years.

To estimate the aerodynamic induced density variation, the research efforts were directed towards using experimental, analytical and numerical methods. The experimental studies^{3,4} addressed the use of extensive instrumentation to statistically quantify the turbulence levels and to provide flow visualization. These experimental parametric studies were conducted for various flow conditions. The primary objective was to estimate the changes in the flowfield fluctuations as a function of small scale turbulence in the shear layer at a selected station. Meanwhile, the experimental scaling laws⁵ were formulated for RMS density fluctuations, transverse scale length and shear layer width with state-of-the-art unsteady aerodynamics and optical measurements. The data for the full scale model was simulated using a compressible boundary layer program. However, the numerical modeling of such three-dimensional problems is preferred because it provides a more detailed description of the flowfield at a lower cost. In order to arrive at the fruitful results, the quantitative analysis of wake structure, separated flow and its domain of influence demand a systematic approach.

Our earlier attempt⁶ was aimed at validating the computational procedure and reconfirming some of the fundamental results for flow past a large protuberance (turret). We were successful in demonstrating the usefulness of a hypothesis that the skin friction lines on the surface are said to behave as a continuous vector

field and the singular points in this field obey the topological rule^{7,8}. This verification also confirmed the primary separation line and horseshoe vortex structure for the surface mounted obstacle, boundary layer interaction⁹. Complementing the efforts, the purpose of the present investigation is to analyze the wake region and to estimate the effect of flow control on the separated flow and the shear layer. The computation is performed using the CRAY-1 computer for a free stream Mach number 0.6 and Reynolds number $12.8 \times 10^6/m$. The compressible Navier-Stokes equations are solved for flow around a hemispherically capped turret mounted on a flat surface. The turret has cutout at an azimuth angle 120° from the free stream direction. The analysis is done for two cases: when the turret is treated as (1) a solid shell and (2) a porous shell with uniform suction rate of 0.136 kg/s. The experimental conditions for the mass suction rate were duplicated by imposing a negative normal velocity component with a magnitude of 3.7 m/s over the porous turret surface. The aim is to evaluate the basic fluid mechanical difference in the flowfield due to mass suction and compare the results with the experimental data^{3,4}.

SECTION 2

GOVERNING EQUATIONS

For classical fluid mechanical problems, the Navier-Stokes equations constitute a very accurate mathematical model. With adequate inclusion of turbulence terms, it provides the basic understanding for the viscous-inviscid interaction and separated flow at high Reynolds number. However, due to computing speed and memory limitation, certain approximations are still needed to use these equations¹⁰.

Applying the fundamental principles of mechanics and thermodynamics for a continuous media in a Galilean (absolute) frame of reference, the integral forms of the conservation law written in the following form¹¹:

Conservation of mass:

$$\frac{d}{dt} \int_{v_t} \rho \cdot dv = 0 \quad (1)$$

Conservation of momentum:

$$\frac{d}{dt} \int_{v_t} \rho \cdot \vec{U} \cdot dv = \int_{\partial v_t} \vec{\sigma} \cdot \vec{n} \cdot ds + \int_{v_t} \rho \cdot \vec{f}_e \cdot dv \quad (2)$$

Conservation of energy:

$$\frac{d}{dt} \int_{v_t} \rho \cdot E \cdot dv = \int_{\partial v_t} (\vec{U} \cdot \vec{\sigma} - \vec{q}) \cdot \vec{n} \cdot ds + \int_{v_t} \rho \cdot \vec{f}_e \cdot \vec{U} \cdot dv \quad (3)$$

where n is the unit normal vector on the surface ∂v_t bounding the volume v_t . These integral forms are supplemented with the constitutive relations for the stress tensor $\vec{\sigma}$ and the heat flux vector \vec{q} in terms of the basic variables:

$$\vec{\sigma} = -p \cdot \vec{I} + \vec{\tau} \quad (4)$$

$$\vec{q} = -k \cdot \text{grad } T \quad (5)$$

where \vec{I} is the unit tensor. In these relations, it is implicitly assumed that the variables ρ , \vec{U} and e are continuous and differentiable.

For turbulent flows, which characterize the large variation in fluid physics, the numerical solutions of the equations (1) through (3) is feasible only if turbulence properties are replaced by some algebraic relations (turbulence model) and the equations are written in a more suitable form. Thus, in the absence of body forces, the unsteady, three-dimensional Navier-Stokes equations, in mass averaged variables and in surface oriented coordinate system, can be written in the convenient form as follows:

$$\frac{\partial \vec{U}}{\partial t} + [\xi_x, \xi_y, \xi_z] \begin{bmatrix} \frac{\partial \vec{F}}{\partial \xi} \\ \frac{\partial \vec{G}}{\partial \xi} \\ \frac{\partial \vec{H}}{\partial \xi} \end{bmatrix} + [\eta_x, \eta_y, \eta_z] \begin{bmatrix} \frac{\partial \vec{F}}{\partial \eta} \\ \frac{\partial \vec{G}}{\partial \eta} \\ \frac{\partial \vec{H}}{\partial \eta} \end{bmatrix} + [\zeta_x, \zeta_y, \zeta_z] \begin{bmatrix} \frac{\partial \vec{F}}{\partial \zeta} \\ \frac{\partial \vec{G}}{\partial \zeta} \\ \frac{\partial \vec{H}}{\partial \zeta} \end{bmatrix} = 0 \quad (6)$$

where

$$\vec{U} = \begin{bmatrix} \rho \\ \rho u \\ \rho v \\ \rho w \\ \rho e \end{bmatrix} \quad (7)$$

$$\vec{F} = \begin{bmatrix} \rho u \\ \rho u^2 + \sigma_x \\ \rho uv + \tau_{xy} \\ \rho uw + \tau_{xz} \\ (\rho e + \sigma_x)u + \tau_{xy} \cdot v + \tau_{xz} \cdot w - \dot{q}_x \end{bmatrix} \quad (8)$$

$$\vec{G} = \begin{bmatrix} \rho v \\ \rho v u + \tau_{yx} \\ \rho v^2 + \sigma_y \\ \rho v w + \tau_{yz} \\ (\rho e + \sigma_y) v + \tau_{yx} \cdot u + \tau_{yz} \cdot w - \dot{q}_y \end{bmatrix} \quad (9)$$

$$\vec{H} = \begin{bmatrix} \rho w \\ \rho w u + \tau_{zx} \\ \rho w v + \tau_{zy} \\ \rho w^2 + \sigma_z \\ (\rho e + \sigma_z) w + \tau_{zx} \cdot u + \tau_{zy} \cdot v - \dot{q}_z \end{bmatrix} \quad (10)$$

$$\sigma_x = p + \frac{2}{3} (\mu + \epsilon) \left(\frac{\partial u}{\partial x} + \frac{\partial v}{\partial y} + \frac{\partial w}{\partial z} \right) - 2(\mu + \epsilon) \cdot \frac{\partial u}{\partial x} \quad (11)$$

$$\tau_{xy} = \tau_{yx} = -(\mu + \epsilon) \left(\frac{\partial u}{\partial y} + \frac{\partial v}{\partial x} \right) \quad (12)$$

$$\tau_{xz} = \tau_{zx} = -(\mu + \epsilon) \left(\frac{\partial u}{\partial z} + \frac{\partial w}{\partial x} \right) \quad (13)$$

$$\sigma_y = p + \frac{2}{3} (\mu + \epsilon) \left(\frac{\partial u}{\partial x} + \frac{\partial v}{\partial y} + \frac{\partial w}{\partial z} \right) - 2(\mu + \epsilon) \cdot \frac{\partial v}{\partial y} \quad (14)$$

$$\tau_{yz} = \tau_{zy} = -(\mu + \epsilon) \left(\frac{\partial v}{\partial z} + \frac{\partial w}{\partial y} \right) \quad (16)$$

$$\sigma_z = p + \frac{2}{3} (\mu + \epsilon) \left(\frac{\partial u}{\partial x} + \frac{\partial v}{\partial y} + \frac{\partial w}{\partial z} \right) - 2(\mu + \epsilon) \cdot \frac{\partial w}{\partial z} \quad (17)$$

$$\dot{q}_x = \gamma \left(\frac{\mu}{Pr} + \frac{\epsilon}{Pr_t} \right) \cdot \frac{\partial e_i}{\partial x} \quad (18)$$

$$\dot{q}_y = \gamma \left(\frac{\mu}{Pr} + \frac{\epsilon}{Pr_t} \right) \cdot \frac{\partial e_i}{\partial y} \quad (19)$$

$$\dot{q}_z = \gamma \left(\frac{\mu}{Pr} + \frac{\epsilon}{Pr_t} \right) \cdot \frac{\partial e_i}{\partial z} \quad (20)$$

$$e = e_i + (u^2 + v^2 + w^2)/2.0 \quad (21)$$

$$e_i = C_v \cdot T \quad (22)$$

For these equations, we assume that the thermodynamic properties of the fluid are governed by the perfect gas law,

$$p = \rho RT \quad (23)$$

with constant specific heat ratio, $\gamma = 1.4$ (air) and the coefficient of viscosity varies with temperature according to the Sutherland's viscosity formula. It is also implied that the thermal conductivity coefficient κ and the viscosity coefficients λ, μ are functions of temperature only and λ, μ comply with the Stoke's relation. The molecular and turbulent Prandtl numbers are assumed to be constant and are equal to 0.72 and 0.90, respectively.

The system of equations (6) through (23) is closed by assigning a specific relation for the coefficient of eddy viscosity.

The fluid motion described by the aforementioned nonlinear, strongly coupled equations is to be analysed around a hemispherically capped turret (Figure 1) mounted on a flat surface. Its base is a circular cylinder with diameter 0.127 meter and height 0.078 meter. The hemispherical dome at the top has a diameter of 0.127 meter whose center is on the turret axis. If we measure the (azimuth) angle clockwise from the oncoming stream direction, the turret has a cutout at 120° AZA at a normal distance 0.057 meter from the turret axis. The origin of the coordinate system is located at the intersection of the turret axis and the flat surface. The ξ, η, ζ directions correspond to axial, normal and tangential transformed coordinates of the turret, respectively. The y-direction corresponds to the turret axis in the Cartesian coordinates (x,y,z).

One of the controlling factors for the numerical simulation is the proper selection of coordinates and grid system. In order

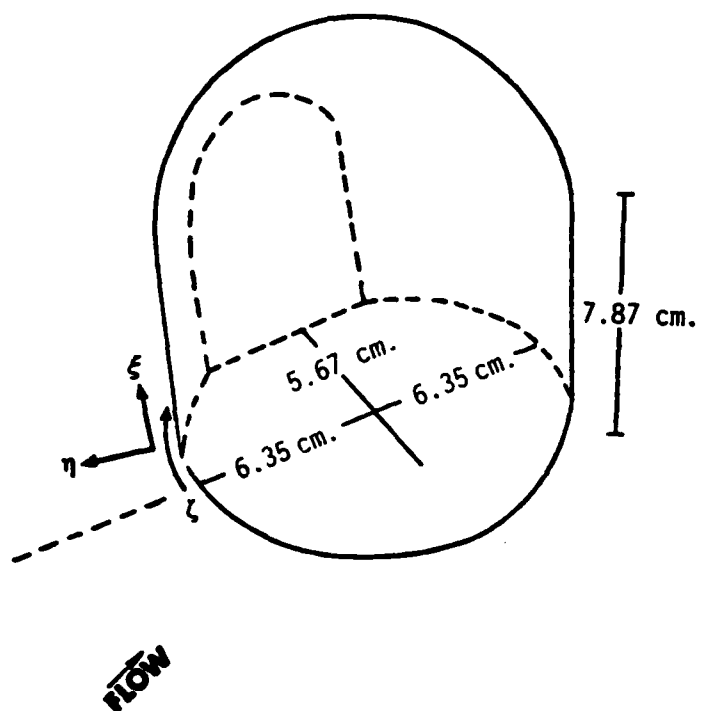


Figure 1. The Turret.

to avoid any interpolation in the transformed computational domain, the effective way is to opt for a turret surface oriented grid system. Since such a system has coordinate lines coinciding with the surface contours of the turret, all boundary conditions can be expressed at the grid points. The normal derivatives at the turret can be represented using only finite difference between grid points on the coordinate lines¹². Thus, we define the turret surface by 62×30 points (Figure 2). On the cylindrical portion, 15 points were used in the axial direction stretched exponentially from the base and 15 points were uniformly placed on the hemispherical dome. In the tangential direction, 62 equidistant points were used with first and last two overlapping points to permit the use of fourth order pressure damping. Using these surface nodes as the reference points, the normal coordinates are then described by 30 exponentially stretched field points (x,y,z) from the turret surface extending outwards to seven times the turret diameter (Figure 3). These points are generated by the homotropy scheme¹³:

$$(x,y,z) = (x,y,z)_{\text{outer}} \cdot \left(\frac{e^{C_N \cdot \eta} - 1}{e^\eta - 1} \right) + (x,y,z)_{\text{turret}} \left(\frac{1 - e^{C_N \cdot \eta}}{e^\eta - 1} \right) \quad (24)$$

where C_N is a nonzero constant. The finer mesh near the turret and flat plate help resolve the viscous effects while the coarser mesh helps to reduce the computational time.

Once the coordinates are generated, the derivatives of coordinate transformation can be obtained through the Jacobian, J

$$J = \frac{\partial(\xi, \eta, \zeta)}{\partial(x, y, z)} = \begin{vmatrix} \frac{\partial x}{\partial \xi} & \frac{\partial y}{\partial \xi} & \frac{\partial z}{\partial \xi} \\ \frac{\partial x}{\partial \eta} & \frac{\partial y}{\partial \eta} & \frac{\partial z}{\partial \eta} \\ \frac{\partial x}{\partial \zeta} & \frac{\partial y}{\partial \zeta} & \frac{\partial z}{\partial \zeta} \end{vmatrix} \quad (25)$$

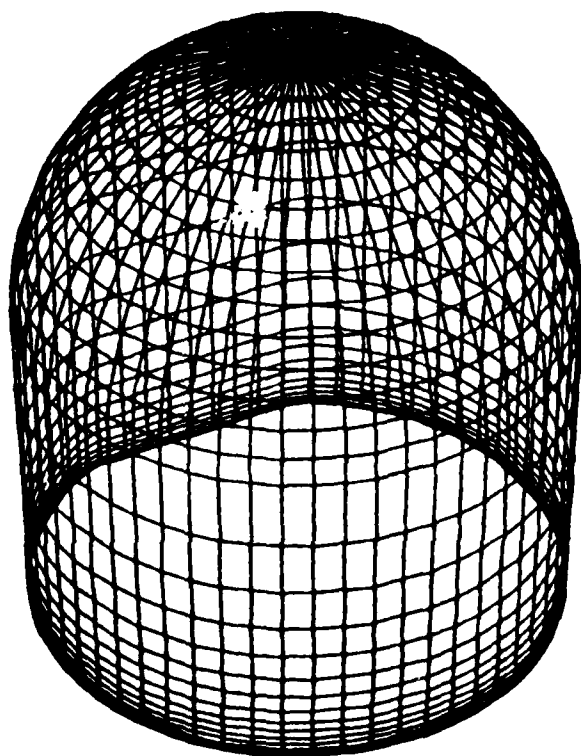


Figure 2. Mesh System of the Turret.

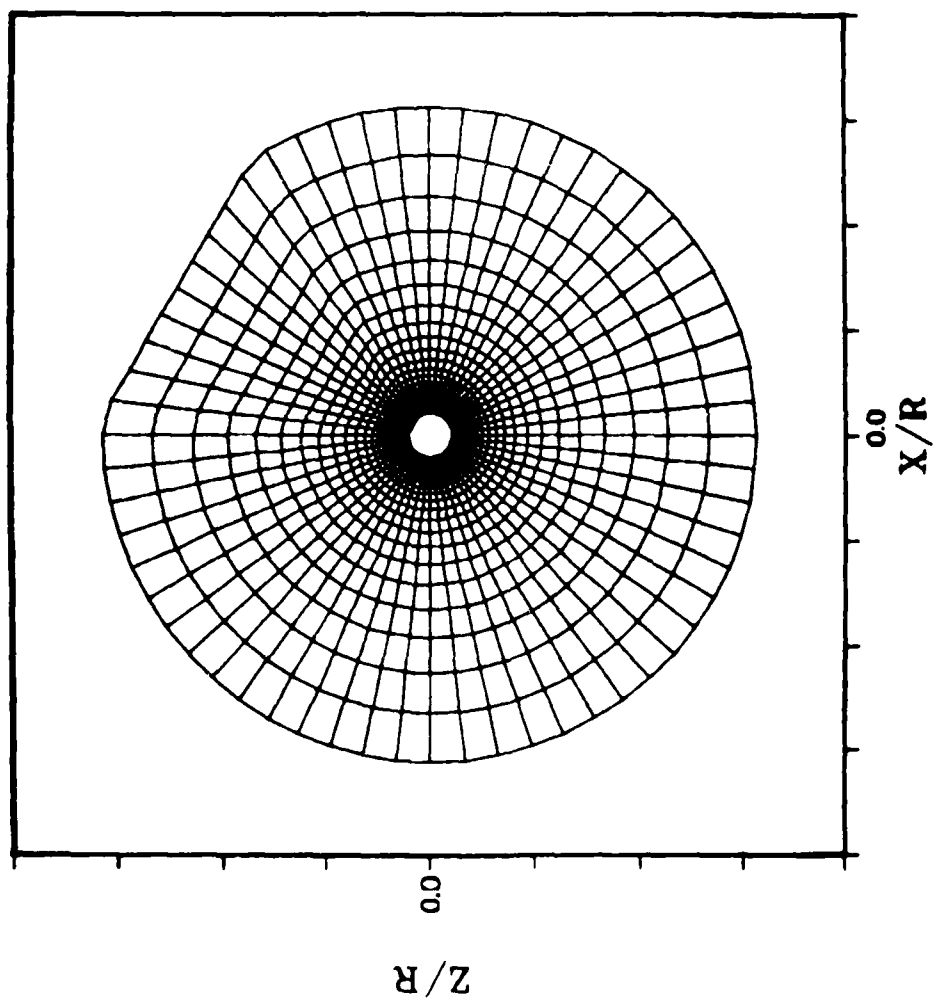


Figure 3. The Mesh Point Distribution on the Flat Surface.

and its inverse

$$J^{-1} = \frac{\partial(x, y, z)}{\partial(\xi, \eta, \zeta)} = \begin{vmatrix} \frac{\partial \xi}{\partial x} & \frac{\partial \eta}{\partial x} & \frac{\partial \zeta}{\partial x} \\ \frac{\partial \xi}{\partial y} & \frac{\partial \eta}{\partial y} & \frac{\partial \zeta}{\partial y} \\ \frac{\partial \xi}{\partial z} & \frac{\partial \eta}{\partial z} & \frac{\partial \zeta}{\partial z} \end{vmatrix} \quad (26)$$

Care has been taken that no mesh point lies on the turret axis. This precaution allows the existence of the inverse Jacobian and permits a one-to-one and onto correspondence from the physical to the transformed space.

For this configuration and the mesh system, our aim is to treat the turret as a solid shell and a porous shell (with uniform mass suction). The basic input for the distributed suction porous shell model is based on the data provided by Haslund³ and Reyhner¹⁴. The maximum flow rate available from the suction pump of 0.136 kg/s was shared as 0.078 kg/s through the hemisphere portion and 0.058 kg/s through the upper half of the cylinder portion (excluding cutout). At a Reynolds number of $12.8 \times 10^6/\text{m}$ and a free stream Mach number 0.6, this suction rate eliminates recirculation between holes¹⁵. For our mesh system, we assume that the suction is being applied to all the grid point locations except at the lower half of the turret and the cutout area. The suction Mach number corresponding to the assigned suction rate is 0.01 which results in a negligible change in turret surface density values.

The well posed and stable boundary conditions for subsonic Navier-Stokes equations are still uncertain. The primary physical phenomenon consisting of the propagation of pressure waves and vortices limit the flow variables to the asymptotic values in the farfield. However, for three-dimensional flows, the relief effect is significant and the disturbances generated by the turret decay rapidly. Thus, if the boundary conditions are specified at a sufficiently large distance from the turret, the overspecification is generally acceptable.

Initially, we assume that the turret is immersed completely in the uniform stream. The upper boundary conditions are the free stream values, whereas at the downstream side, the gradient of the flow properties is assumed to vanish. On the solid surfaces, the noslip condition for the velocity component along with prescribed wall temperatures are imposed, while near the turret axis, an interpolation is adopted to eliminate calculation on this singularity. Along the coinciding plane (azimuth angles 0° and 360°), the conditions were matched at all the mesh points. Or, in other words, the following initial and boundary conditions were applied on the unit cube (Figure 4) in the transformed space $0 \leq \xi, \eta, \zeta \leq 1.0$.

Initial Conditions

$$\vec{U}(0, \xi, \eta, \zeta) = \vec{U}_\infty \quad (27)$$

Boundary Conditions

$$\text{Upstream: } \vec{U}(t, \xi, 1, \zeta_0) = \vec{U}_\infty, \quad \begin{array}{l} \zeta_0 < \zeta_2 \\ \zeta_0 > 1 \end{array} \quad (28)$$

where ζ_0 is a particular value of ζ corresponding to all the grid points facing the upcoming flow (ζ_2 corresponds to the azimuth angle 90° and ζ_1 for the azimuth angle 270°).

$$\text{Downstream: } \left. \frac{\partial}{\partial \eta} \vec{U}(t, \xi, \eta, \zeta_0) \right|_{\eta=1} = 0, \quad \zeta_2 \leq \zeta \leq \zeta_1 \quad (29)$$

$$\begin{aligned} \text{On the solid surfaces: } u = v = w = 0 \\ T_w = 1.0695 \cdot T_\infty \\ \frac{\partial P}{\partial \vec{\eta}} = 0 \end{aligned} \quad (30)$$

where $\vec{\eta}$ is the direction normal to the solid surfaces.

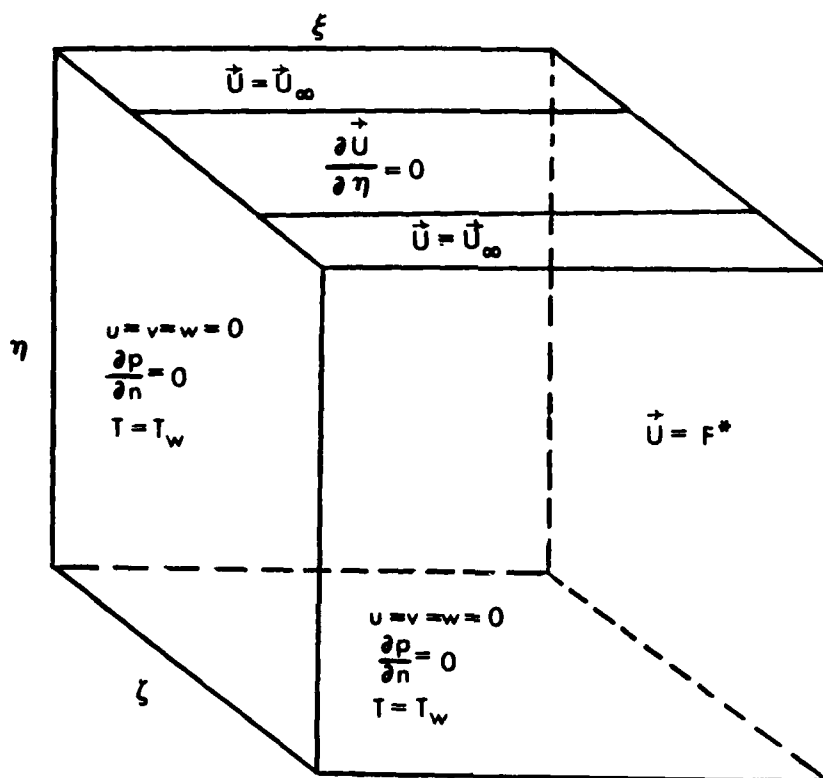


Figure 4. The Boundary Conditions.

Near the turret axis: $\vec{U}(t, l, \eta, \zeta) = \text{IPF}$ (31)

where

$$\text{IPF} = \frac{ds_2}{2(ds_1 + ds_2)} \cdot \vec{U}(t, l - \Delta\xi, \eta, \zeta + 30 \cdot \Delta\zeta) + \frac{ds_2 + 2 ds_1}{2(ds_1 + ds_2)} \times \vec{U}(t, l - \Delta\xi, \eta, \zeta). \quad (32)$$

It may be recalled that there are 60 equidistant mesh points in the tangential direction and $\zeta + 30 \cdot \Delta\zeta$ will identify the diagonally opposite mesh point across the turret axis. The terms ds_1 and ds_2 are the arc lengths subtended by the mesh points (l, η, ζ) and $(l - \Delta\xi, \eta, \zeta)$ along the turret axis to the center of the hemisphere (turret top).

These are the boundary conditions when the turret is treated as a solid shell. For the computation with mass suction, the boundary conditions at the porous turret surface are replaced by the negative normal velocity component of magnitude 3.7 m/s.

SECTION 3 TURBULENCE MODEL

The algebraic eddy viscosity model used in this study is due to Baldwin and Lomax¹⁶. The model is tailored particularly to suit the wake region at the turret shoulder where substantial variation in all the three directions dominates. It is described briefly as follows:

In the inner region, the eddy viscosity is given by

$$\epsilon_i = (k_1 \cdot L \cdot D_1)^2 \cdot \rho \cdot |\omega| \quad (33)$$

where $k_1 = 0.4$ is the von Karman's constant, D_1 is the van Driest's damping factor,

$$D_1 = 1 - \exp \left(- \sqrt{\frac{\rho_w \cdot |\omega_w|}{\mu_w}} \cdot \frac{L}{26} \right) \quad (34)$$

and ω is the vorticity function (Appendix). The scale length L , is the distance normal to the turret or the flat plate surface (Figure 5):

$$L = \min \begin{cases} \sqrt{(x-x_T)^2 + (y-y_T)^2 + (z-z_T)^2} \\ (y-y_{FL}) \end{cases} \quad (35)$$

where (x,y,z) are the Cartesian coordinates of the field point, $(x,y,z)_T$ and $(x,y,z)_{FL}$ are the projection coordinates on the turret and flat plate surface, respectively. This relation agrees with the asymptotic length scale formulation¹⁷.

In the wake region:

$$\epsilon_o = C_c \cdot C_A \cdot F_{WAKE} \cdot F_{KIF}. \quad (36)$$

The Clauser constant $C_c = 0.0168$ is multiplied by an additional constant, $C_A = 1.6$ and the coefficient, F_{WAKE} , is given by

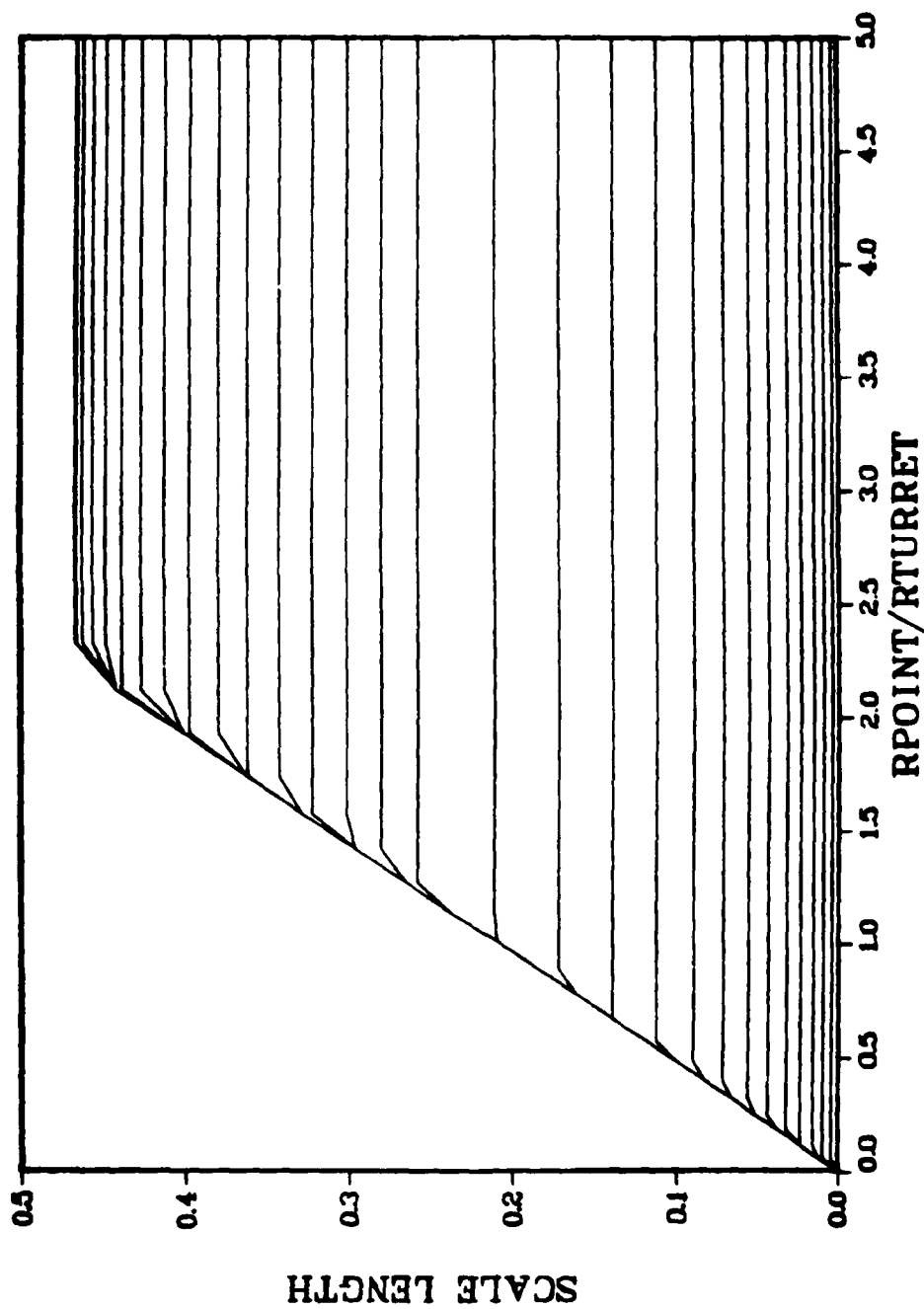


Figure 5. Scale Lengths for the Turbulence Model.

$$FWAKE = \min \begin{cases} L_{\max} \cdot TF_{\max} \\ 0.25 \cdot L_{\max} \cdot UD^2 / TF_{\max} \end{cases} \quad (37)$$

The scale length L_{\max} is a particular value of L when the function $TF(=L \cdot |\omega|)$ attains its maximum, TF_{\max} . The introduction of the function TF in this turbulence model poses certain difficulties in uniquely defining the maximum value or "the peak". In the turret wake region, this function strongly depends on vorticity. Due to large-scale oscillatory flow, the function TF is expected to have more than one peak^{18,19}. These peaks display a "double-hump" like character causing an abrupt change in L_{\max} . Thus, during our computation, we always take the first peak to avoid an inconsistency and possible mutilation in the final results. The other terms included are the Klebanoff intermittancy correction factor, FKIF.

$$FKIF = \left[1.0 + 5.5 \left(0.3 \cdot \frac{L}{L_{\max}} \right)^6 \right]^{-1} \quad (38)$$

and the total velocity differential, UD

$$UD = \sqrt{u^2 + v^2 + w^2} \Big|_{\max} - \sqrt{u^2 + v^2 + w^2} \Big|_{\min} \quad (39)$$

The effective viscosity is, then, taken to be

$$\epsilon = \min(\epsilon_i, \epsilon_o). \quad (40)$$

SECTION 4 NUMERICAL PROCEDURE

Owing to the large memory availability and high data processing rate (the CPU time per grid point per time iteration), the computer CRAY-1 was chosen for our computation. The well-established vector solver²⁰ was the natural choice to utilize the MacCormack's explicit finite difference scheme²¹. For this scheme, the computation for one time step can be accomplished through the following simple functional relation:

$$U_{i,j,k}^{n+1} = L^*(\Delta t) \cdot U_{i,j,k}^n \quad (41)$$

where the differencing operator, $L^*(\Delta t)$, is given by

$$L^*(\Delta t) = L_{\xi}^*(\Delta t) + L_{\eta}^*(\Delta t) + L_{\zeta}^*(\Delta t) \quad (42)$$

and

$$U_{i,j,k}^n = \vec{U}(\eta \cdot \Delta t, i \cdot \Delta \xi, j \cdot \Delta \eta, k \cdot \Delta \zeta). \quad (43)$$

This form of unsplit algorithm exploits the fundamental characteristics of the CRAY-1 system, in that it operates on a single memory path. This results in a substantial saving on memory loading and we achieve the same final results with further reduction in data processing rate.

Since MacCormack's scheme is conditionally stable²², in order to avoid catastrophic instability, the Courant-Fredrich-Lewy (CFL) condition must be satisfied. For the turret oriented coordinate system, the allowable time increment derived from the stability analysis can be given by:

$$\begin{aligned}
\Delta t_{\text{CFL}} = & \left\{ \left[\frac{U_{\xi}}{\Delta \xi} + \frac{U_{\eta}}{\Delta \eta} + \frac{U_{\zeta}}{\Delta \zeta} \right] + c \cdot \left[\left(\frac{\partial \xi}{\partial x} \cdot \frac{1}{\Delta \xi} + \frac{\partial \eta}{\partial x} \cdot \frac{1}{\Delta \eta} + \frac{\partial \zeta}{\partial x} \cdot \frac{1}{\Delta \zeta} \right)^2 \right. \right. \\
& + \left(\frac{\partial \xi}{\partial y} \cdot \frac{1}{\Delta \xi} + \frac{\partial \eta}{\partial y} \cdot \frac{1}{\Delta \eta} + \frac{\partial \zeta}{\partial y} \cdot \frac{1}{\Delta \zeta} \right)^2 \\
& \left. \left. + \left(\frac{\partial \xi}{\partial z} \cdot \frac{1}{\Delta \xi} + \frac{\partial \eta}{\partial z} \cdot \frac{1}{\Delta \eta} + \frac{\partial \zeta}{\partial z} \cdot \frac{1}{\Delta \zeta} \right)^2 \right]^{0.5} \right\}^{-1}
\end{aligned} \tag{44}$$

where the velocity components are defined as

$$\begin{aligned}
U_{\xi} &= \frac{\partial \xi}{\partial x} \cdot u + \frac{\partial \xi}{\partial y} \cdot v + \frac{\partial \xi}{\partial z} \cdot w \\
U_{\eta} &= \frac{\partial \eta}{\partial x} \cdot u + \frac{\partial \eta}{\partial y} \cdot v + \frac{\partial \eta}{\partial z} \cdot w \\
U_{\zeta} &= \frac{\partial \zeta}{\partial x} \cdot u + \frac{\partial \zeta}{\partial y} \cdot v + \frac{\partial \zeta}{\partial z} \cdot w
\end{aligned} \tag{45}$$

The CFL number is generally in the range of 0.0 and 1.0. However, a conservative choice of Courant-Fredrich-Lewy (CFL = 0.8) condition was implemented to have optimum time step with stable numerical evolution.

We use the solver²⁰ to initialize the planes or "pages" in the (η - ζ) planes and to sweep, for each time step, in the ξ -direction. The vector length for the present case was 62 which is also the longest index array of the three-dimensional mesh system. The computational facilities were utilized with remote access via long distance dial-up and the SAMNET network. Before starting the final computation, we solved the governing equations (6) through (23) together with the initial and boundary conditions (27) through (32) for the first one hundred time steps at low CFL number. The object was to select the proper mesh sizes and to estimate the data processing rate. Our parameters were exponentially stretching the coefficient along the normal direction from the turret and

flat surfaces and the location of the outer boundary. The results are presented in Table 1. The best choice for the coefficients was 1.25 (normal to the flat surface), 5.0 (normal to the turret surface) and 7.0 (the location of the outer boundary). The finer mesh sizes were $1.12 \times 10^{-3} \text{m}$ and $0.906 \times 10^{-3} \text{m}$, respectively, and the angular displacement between nodes was 6° . These mesh sizes seem to provide satisfactory time step increment during computation. Further refinement resulted in a stiffen behavior of the transformation metric elements or unrealistic time step. For these mesh sizes, the data processing rate improved as the computation advanced. The final value achieved for the data processing rate was 4.8×10^{-5} seconds.

Finally, to eliminate the unwanted numerical oscillations in the computational domain, the artificial viscosity terms are included in our solution procedure. For this purpose, the fourth order pressure damping terms as rationalized by MacCormack²² were implemented. In each sweep direction, these expressions are of the form:

$$\begin{aligned}
 & \beta \cdot \Delta t \cdot \Delta \xi^3 \cdot \left[\left| \frac{\partial U}{\partial \xi} \right| + \left\{ \left(\frac{\partial \xi}{\partial x} \right)^2 + \left(\frac{\partial \xi}{\partial y} \right)^2 + \left(\frac{\partial \xi}{\partial z} \right)^2 \right\}^{1/2} \cdot C \right] \cdot \frac{1}{P} \cdot \left| \frac{\partial^2 P}{\partial \xi^2} \right| \\
 & \beta \cdot \Delta t \cdot \Delta \eta^3 \cdot \left[\left| \frac{\partial U}{\partial \eta} \right| + \left\{ \left(\frac{\partial \eta}{\partial x} \right)^2 + \left(\frac{\partial \eta}{\partial y} \right)^2 + \left(\frac{\partial \eta}{\partial z} \right)^2 \right\}^{1/2} \cdot C \right] \cdot \frac{1}{P} \cdot \left| \frac{\partial^2 P}{\partial \eta^2} \right| \\
 & \beta \cdot \Delta t \cdot \Delta \zeta^3 \cdot \left[\left| \frac{\partial U}{\partial \zeta} \right| + \left\{ \left(\frac{\partial \zeta}{\partial x} \right)^2 + \left(\frac{\partial \zeta}{\partial y} \right)^2 + \left(\frac{\partial \zeta}{\partial z} \right)^2 \right\}^{1/2} \cdot C \right] \cdot \frac{1}{P} \cdot \left| \frac{\partial^2 P}{\partial \zeta^2} \right|
 \end{aligned} \tag{46}$$

The values for the coefficient β were between two and four. These damping terms were significant only in the region of high pressure oscillations.

Once the initial phase of computation was completed and some anticipated periodicity in the flow variables was observed, the analysis of density fluctuations and wake structures was attempted to compute the correlation coefficient along 120° AZA.

TABLE 1
RESULTS OF EXPONENTIALLY STRETCHING THE COEFFICIENT

Stretching Parameter		Outer Boundary	$\left(\frac{\Delta y}{R}\right)_{\min} \times 10^2$ 1 ft.	$\left(\frac{\Delta x}{R}\right)_{\min} \times 10^2$ 1 ft.	$\frac{\partial n}{\partial x}$	Time, sec. $\times 10^7$
Normal to Plate	Normal to Turret					
1.25	4.5	5 D	1.4263	1.6803	21.0	1.625
1.25	5.0	5 D	1.4263	1.2378	30.8	1.263
1.25	5.5	5 D	1.4263	0.7681	46.6	0.926
1.22	5.0	5 D	1.7969	1.2378	30.8	1.324
1.50	4.5	5 D	0.2112	1.6803	20.8	0.454
1.22	4.5	5 D	1.7969	1.6803	21.0	1.741
1.22	8.0	5 D	1.7969	0.0960	410.0	0.131
1.20	4.5	7.5 D	0.206	2.6404	12.0	2.425
1.25	5.0	7.5 D	1.4263	1.7763	20.4	1.683
1.80	4.5	10 D	0.0264	3.6006	10.08	0.0695
1.22	4.5	10 D	1.7969	3.6006	10.08	2.554

SECTION 5

RESULTS AND DISCUSSION

Before evaluating the various aspects of our computed results, we present a brief justification for the first peak, in the calculation of the wake function, referred to in the turbulence model.

The prime motivation behind improving Cebeci's²³ formulation was to avoid computing the outer edge of the boundary layer. In the present model¹⁶, instead of solving the displacement thickness integral, the distribution of vorticity is used to determine the length scale. For the time dependent calculation, the function, $TF(=L \cdot |\omega|)$ depends strongly on the vorticity which sheds periodically in the downstream direction. This fact is illustrated in Figures 6 through 8, where the function is plotted against the nodal point location along the normal direction of the turret shoulder. The instantaneous-functional values at the azimuth angles 120° AZA (Figure 6), 180° AZA (Figure 7) and 240° AZA (Figure 8) are picked up to demonstrate the typical behavior. It is certain that a serious difficulty is posed to uniquely and consistently define TF_{\max} (and, therefore, L_{\max}), if the true maximum of TF is taken. As the vortices develop and shed, the constant TF_{\max} (shown in the figures by a solid point) changes its magnitude and location (L_{\max}) abruptly. This induces a substantial error in computing ϵ_0 . In order to avoid such irregularity, we always take first peak of the function TF as TF_{\max} .

In Figure 9 we given the value of TF_{\max} along the azimuth angle 0° through 360° at the turret shoulder. It can be observed that in the downstream direction, for the azimuth angles 90° through 270°, the function TF_{\max} is bounded to a reasonable limit even though the time dependent variation exhibits a marked difference. (This limit was four-folds larger when the true maximum was taken.) Such consideration ascertained a convincing definition of eddy viscosity coefficient ϵ , as shown in Figure 10. The

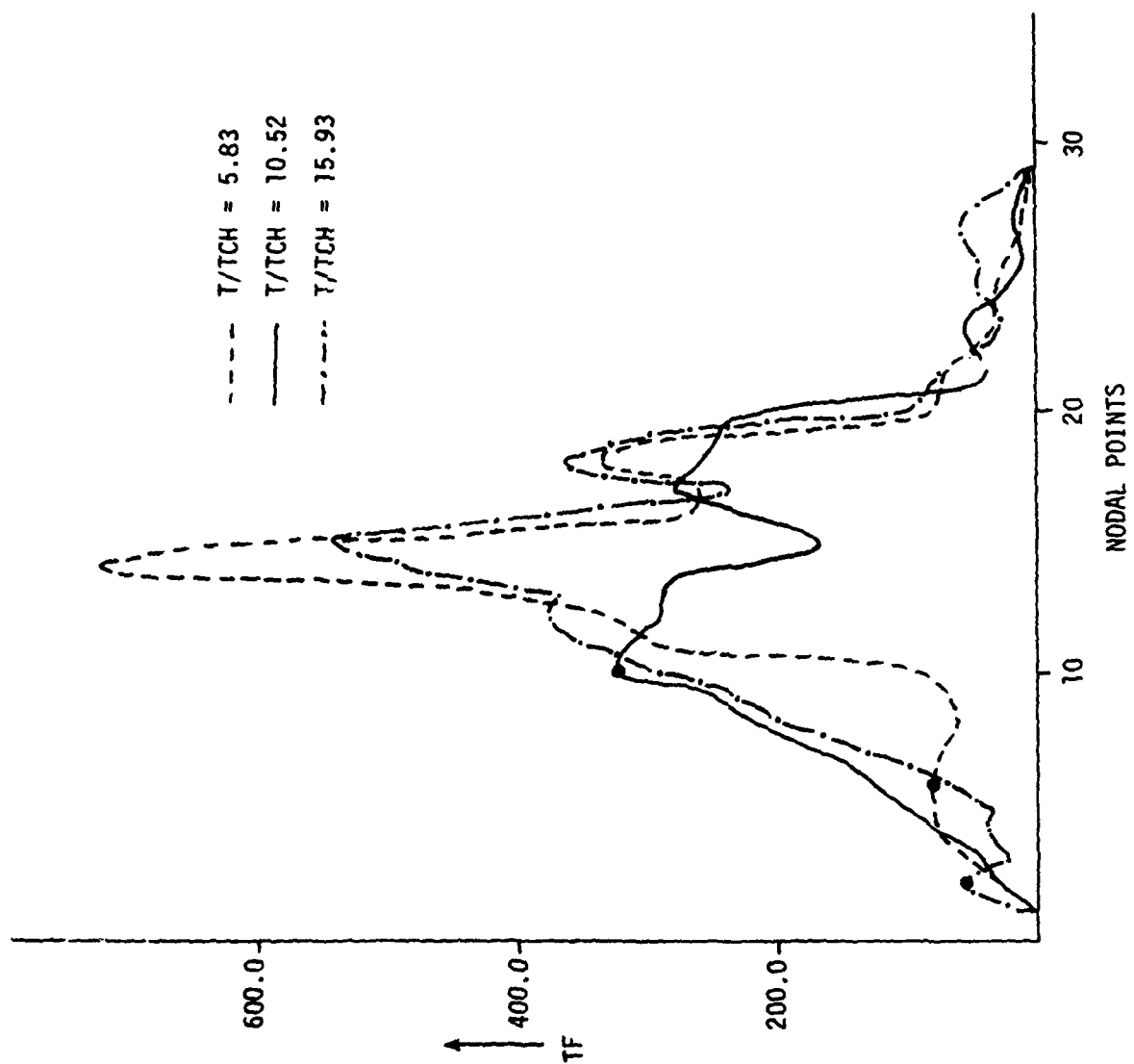


Figure 6. The Function TF Along 120° AZA.

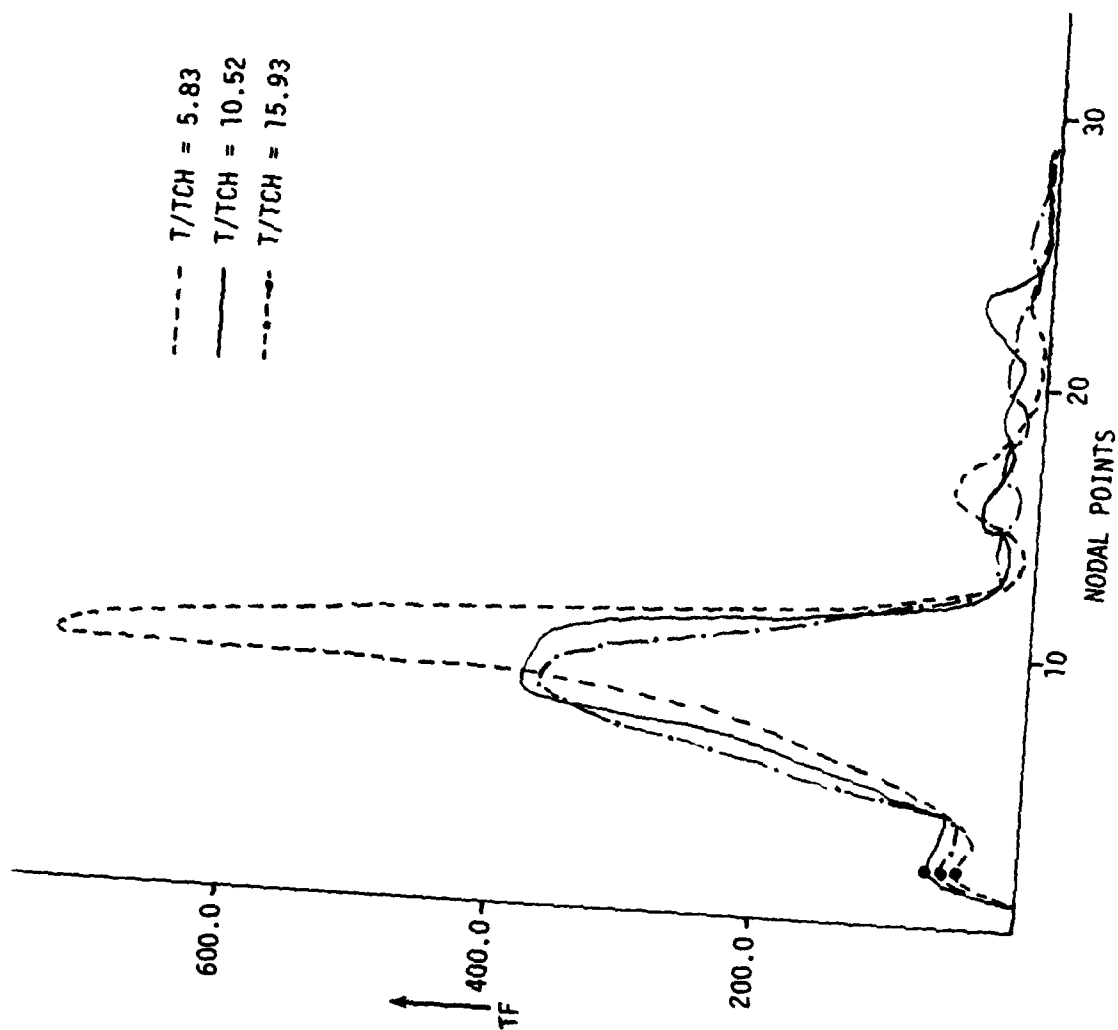


Figure 7. The Function TF Along 180° AZA.

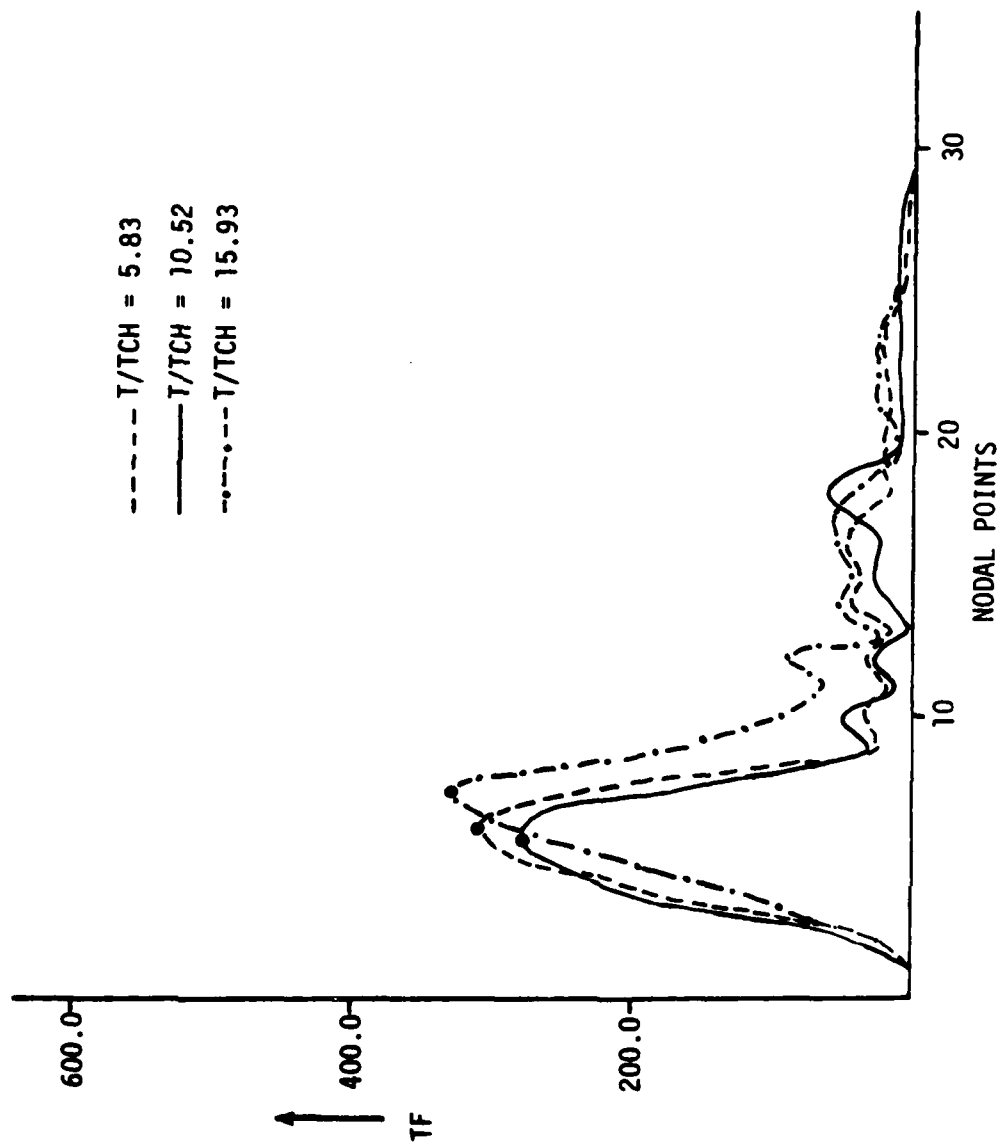


Figure 8. The Function TF Along 240° AZA.

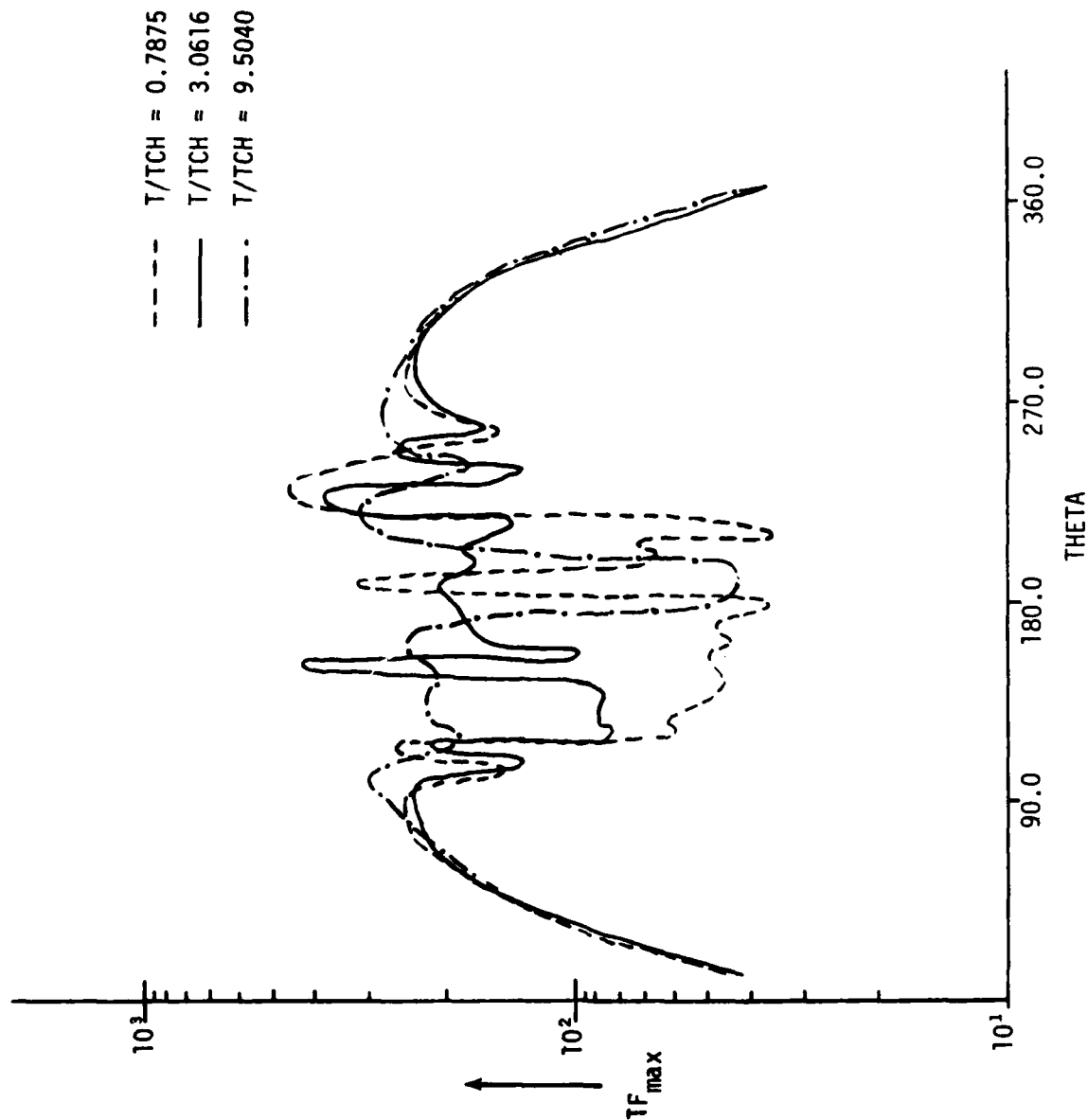


Figure 9. The Coefficient TF_{max} for Various Time Levels.

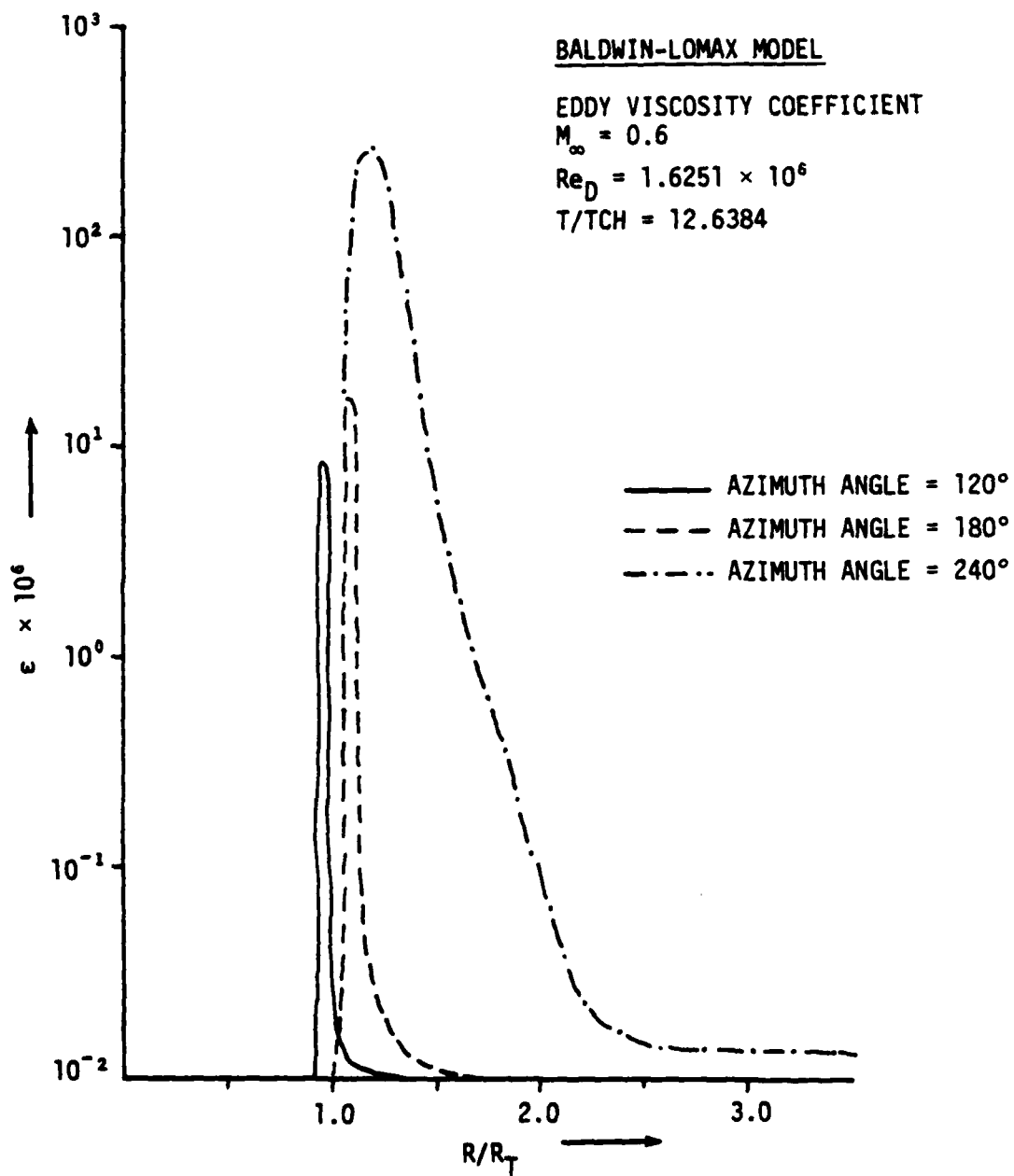


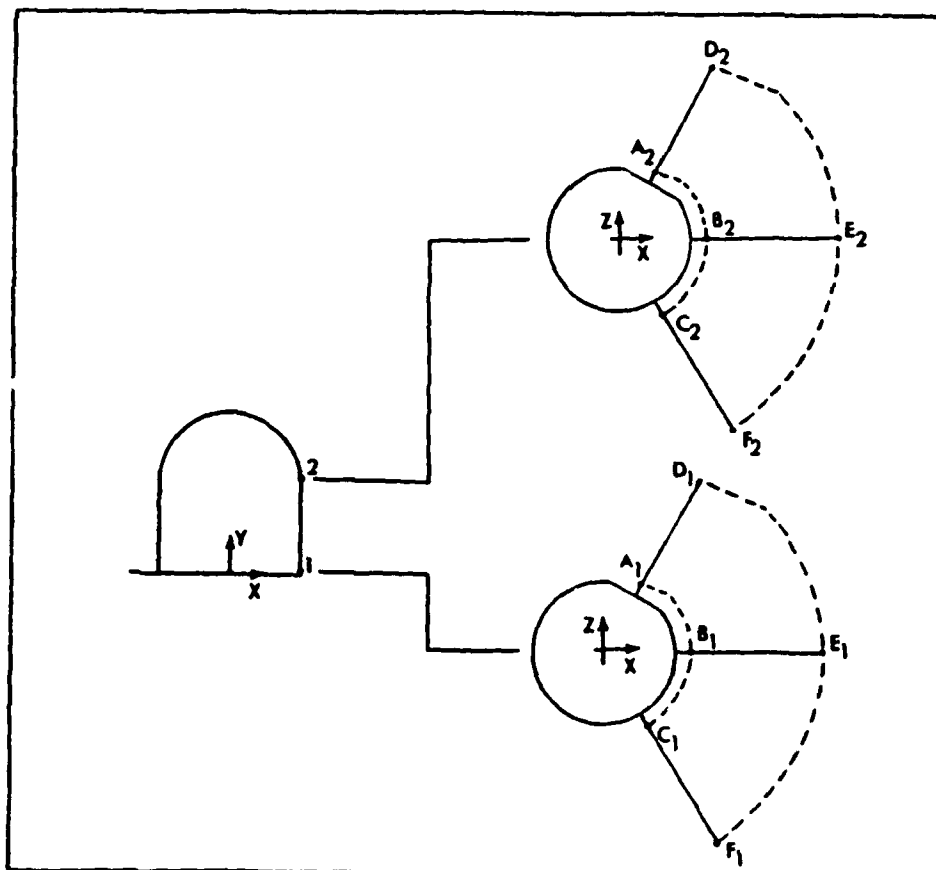
Figure 10. The Eddy Viscosity Coefficient.

normal distance R is normalized by the turret radius R_T . The effective eddy viscosity is within one turret radius and remained in this range throughout our computation.

During the computation we recorded the pressure and Mach number variation at twelve different locations in the wake region (Figure 11). The points in the plane were equally distributed in the planes parallel to the flat surface at heights $Y/R = 1.427 \times 10^{-2}$ (close to the flat plate) and $Y/R = 1.2304$ (at the turret shoulder). Figures 12 to 14 give pressure variation at some of these locations for the cases (1) without suction; and (2) with suction. It is evident that the pressure oscillations reduce considerably, in particular farther from the turret, for the flow with suction. This feature also indicates, as we shall discuss later, that the flow with suction should be well organized for the large-scale motion.

For numerical solution, the comparison with experimental data provides the validation of the computational procedure as well as guidelines for the subsequent analysis. The experimental results^{3,4} relevant to our study are essentially parametric in nature and offer the basic measurements at selected stations.

The pressure coefficient distributions at the turret shoulder are presented for the cases without suction (Figure 15) and with suction (Figure 16). The variable THETA is the azimuth angle measured in the clockwise direction from the oncoming free stream. The different curves represent the pressure coefficient variation during one principal time period. The mean value agrees quite well with the experimental data³. This agreement improves for the flow with suction, particularly around 270° AZA. It is important to note that the presence of the cutout, from azimuth angles 96° to 144° has not affected the pressure coefficient, as it is already immersed in the separated flow. This hints that the cutout does not influence the upstream separation mechanism irrespective of the flow conditions at the turret surface. In the wake region, from 120° AZA to 240° AZA, the pressure recovery is faster and



$$A_{1,2} = (1.099.R, 120.0^\circ)$$

$$B_{1,2} = (1.099.R, 180.0^\circ)$$

$$C_{1,2} = (1.099.R, 240.0^\circ)$$

$$D_{1,2} = (3.436.R, 120.0^\circ)$$

$$E_{1,2} = (3.436.R, 180.0^\circ)$$

$$F_{1,2} = (3.436.R, 240.0^\circ)$$

Figure 11. Typical Mesh Point Location.

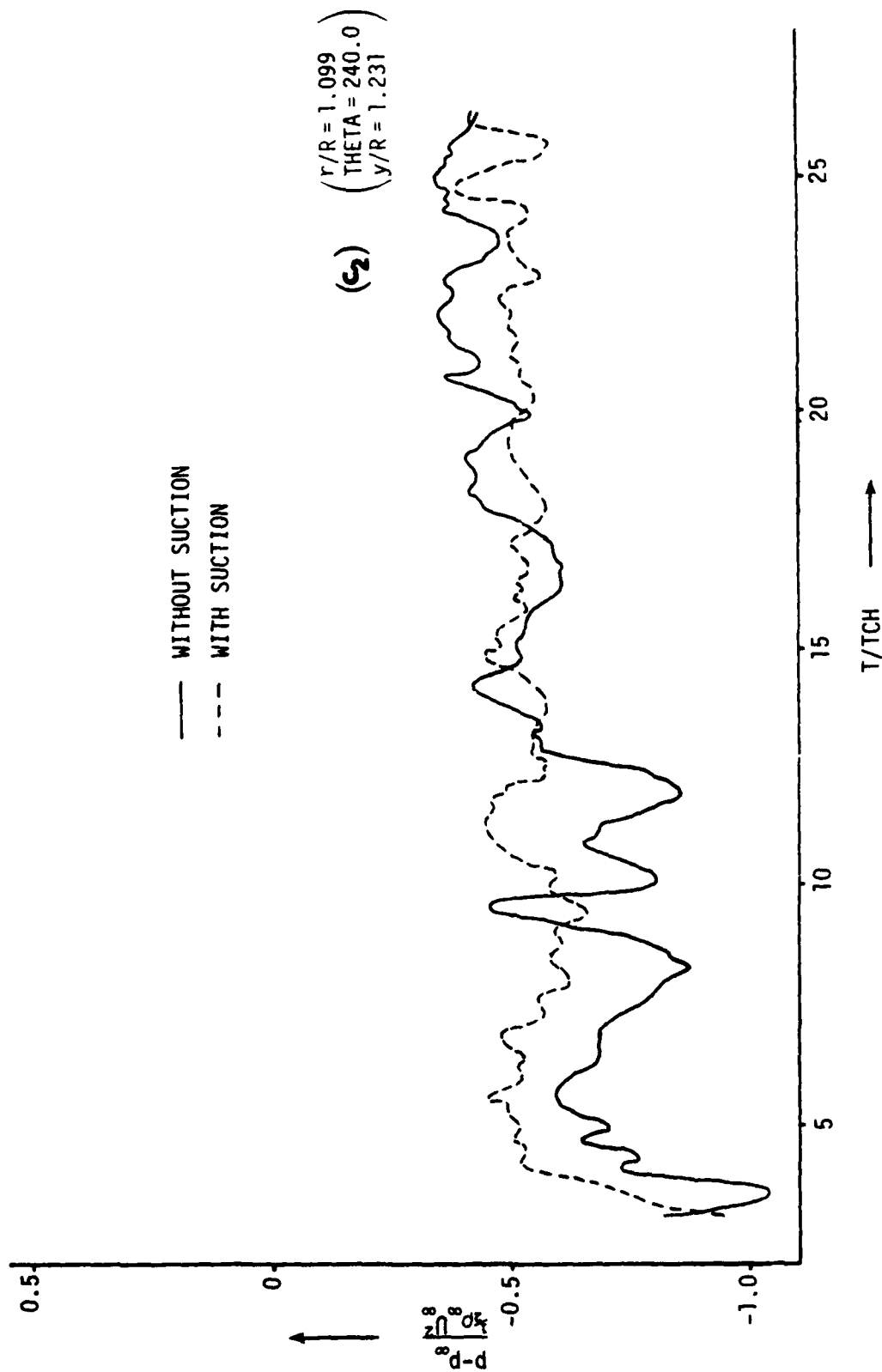


Figure 12. Pressure Coefficient at $\frac{y}{R} = 1.2394$, (C₂).

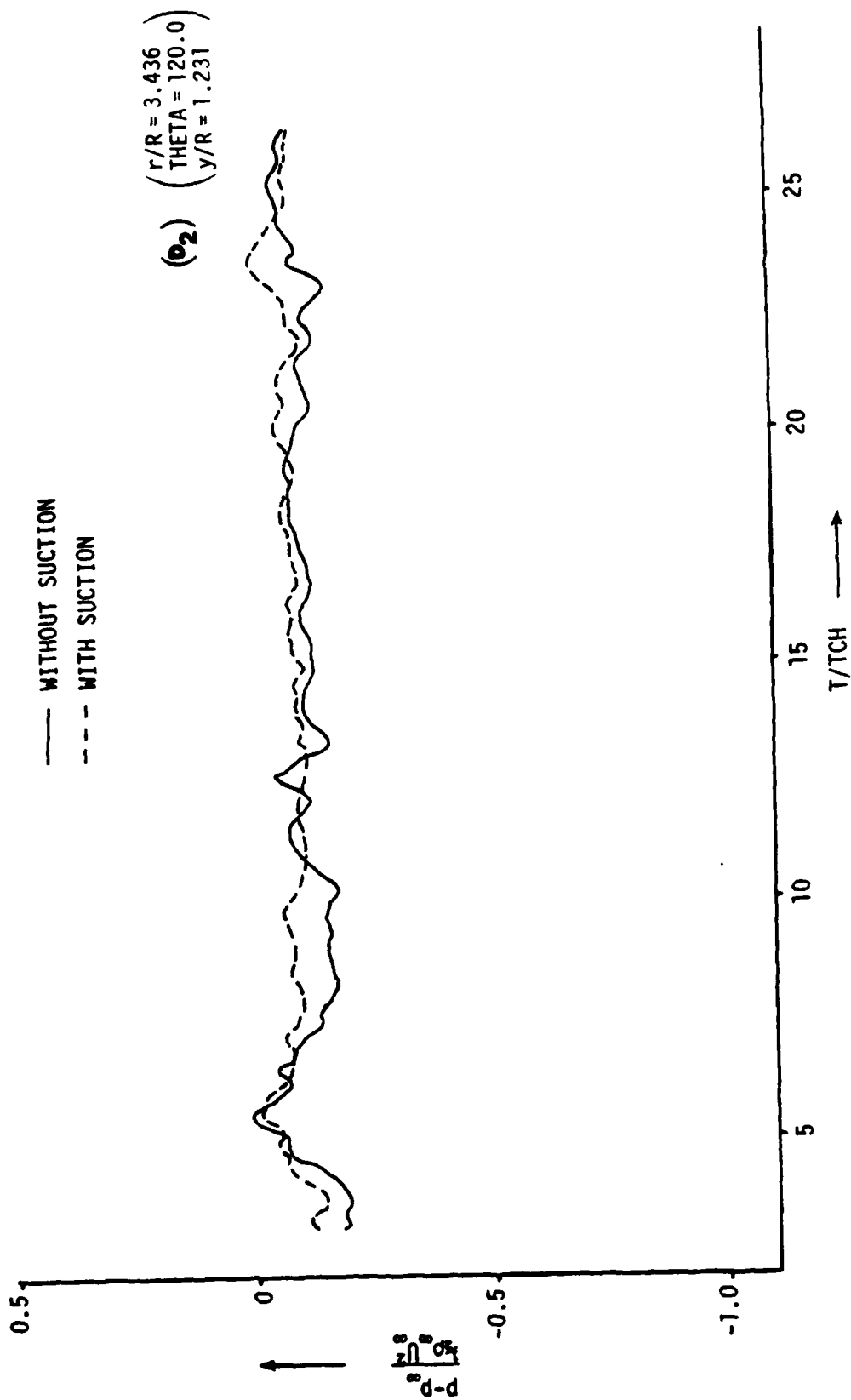


Figure 13. Pressure Coefficient at $\frac{Y}{R} = 1.2394$, (D_2) .

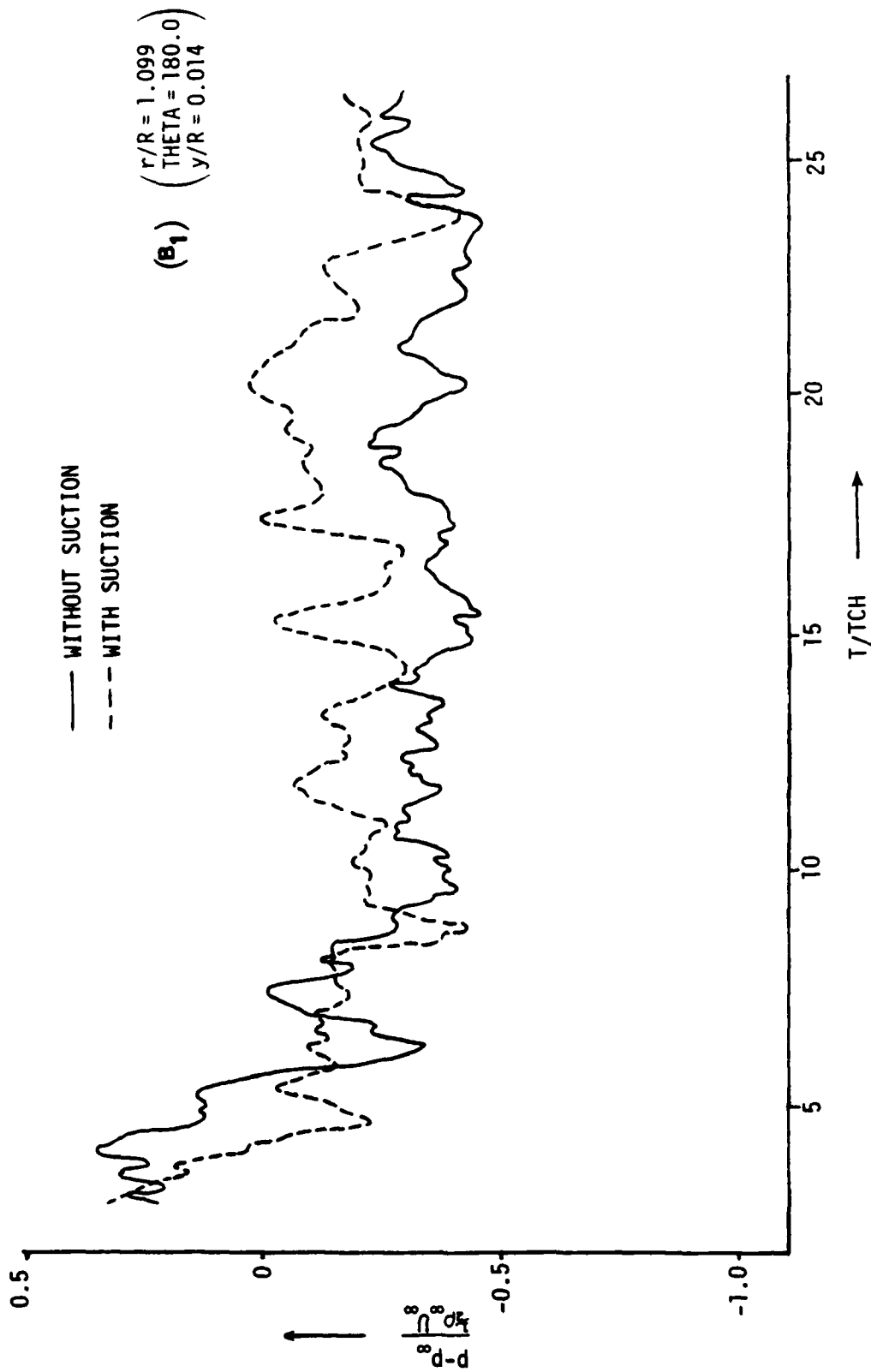


Figure 14. Pressure Coefficient at $\frac{y}{R} = 1.627 \times 10^{-2}$, (B₁).

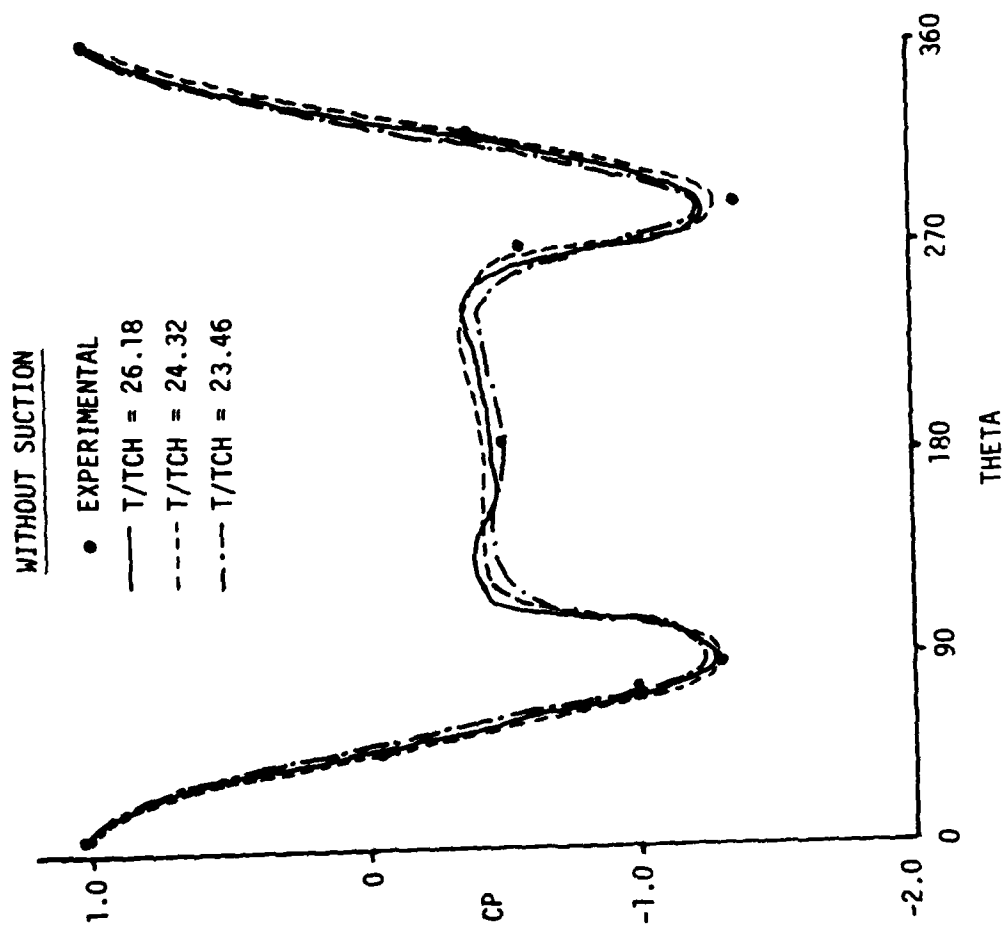


Figure 15. Comparison of Pressure Distribution for Flow Without Suction.

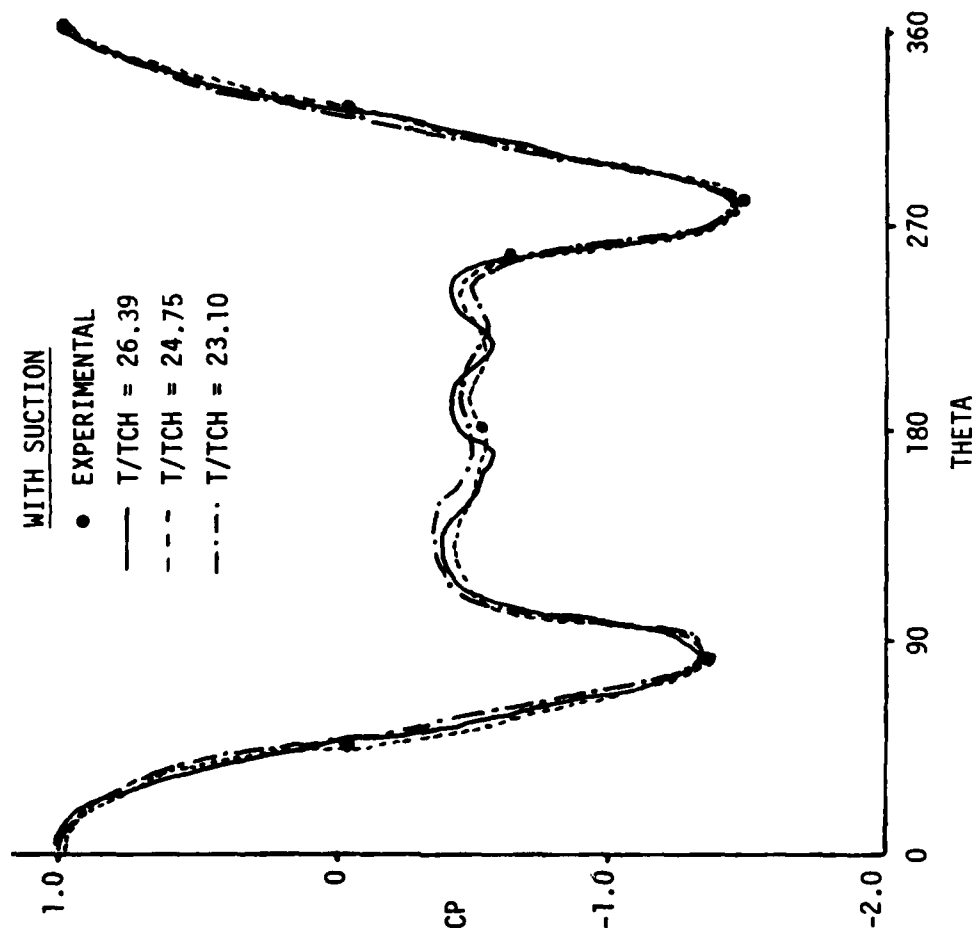


Figure 16. Comparison of Pressure Distribution for Flow With Suction.

the turret surface experiences pronounced pressure variation for the flow with suction. It can be interpreted as if along the rear stagnation line, there is a tendency for the flow to reattach and in this vicinity, the separation effects are stronger.

We also compare, in Figures 17 to 19, the Mach number variations in the rear wake regions for the flow without and with suction. The experimental value is available only along the azimuth angle 120° AZA at the point A_2 . The characteristic time, TCH, is the ratio of the turret diameter and free stream velocity. The mean local Mach number value approaches asymptotically to the time averaged experimental measurements⁴ for both the cases (Figure 17). For the flow with suction, the time dependent variation as well as the mean value are higher than their counterpart. This fact suggests that a small uniform suction rate of 0.135 kg/s eliminates most of the retarded fluid particles and it intensifies the vortical motion in the wake.

This argument is further confirmed in Figure 20 which shows the velocity field in the turret shoulder plane for the flow without suction. As the turret cutout is entirely within the separated flow, it does not cause any amplification to the process of vortex shedding. On the contrary, a small separation bubble appears to fill in for the surface deflection and the oscillatory flow behaves, qualitatively, like flow past a circular cylinder²⁴. To represent the wake structure in a proper perspective, a simple interpolation is used to transform the computed results from the body oriented coordinate system (γ, θ) to the Cartesian coordinate system (x, z) . To illustrate this procedure, we take four mesh points, 1, 2, 3, 4, which are nearest to the Cartesian coordinate system point '5' (Figure 21). With the help of simple geometry, the curvilinear coordinates (γ_5, θ_5) of the point '5' can be found. While the fluid properties (FP) at the points (γ_1, θ_1) , (γ_2, θ_2) , (γ_3, θ_3) and (γ_4, θ_4) are known, by virtue of solving complete Navier-Stokes equations, the fluid properties (velocity, density, Mach number, etc.) can be computed at the point (γ_5, θ_5) by using the following relation.

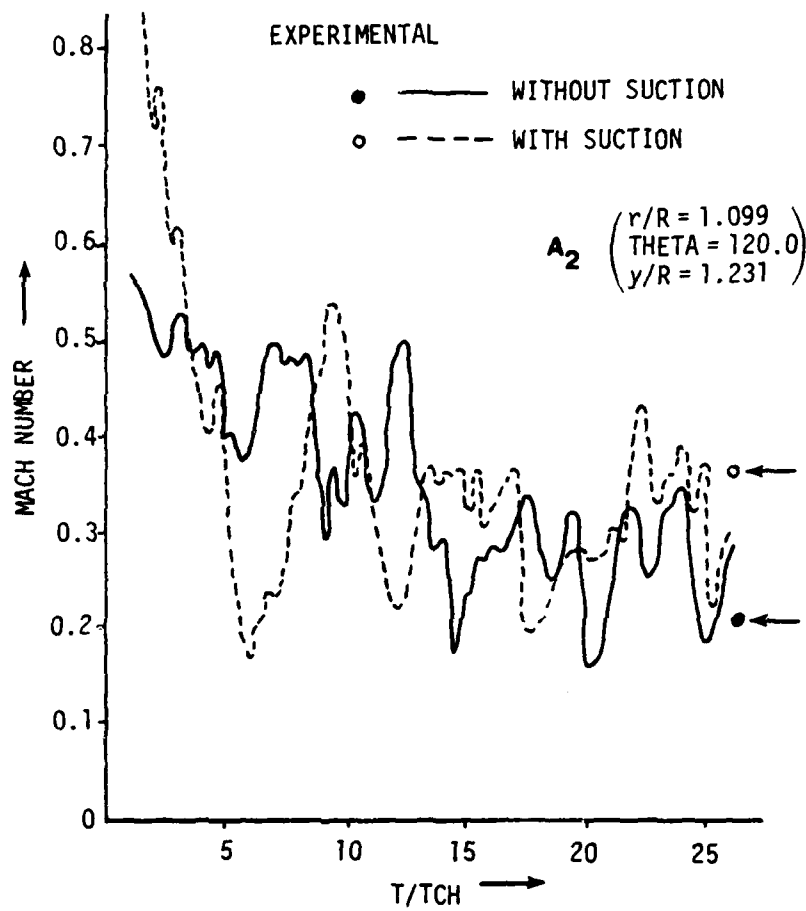


Figure 17. Local Mach Number Variation at Mach Point A_2 .

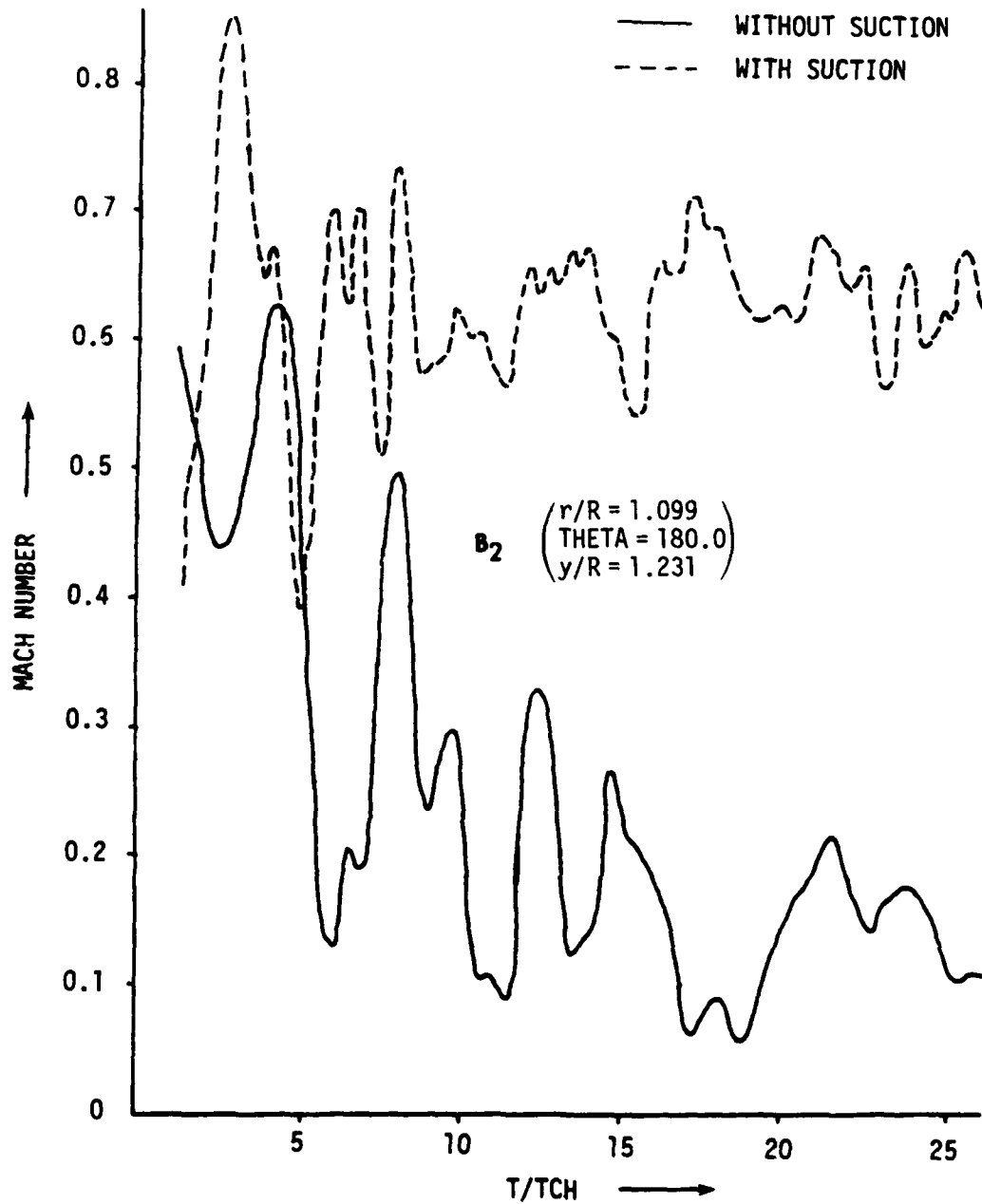


Figure 18. Local Mach Number Variation at Mesh Point B_2 .

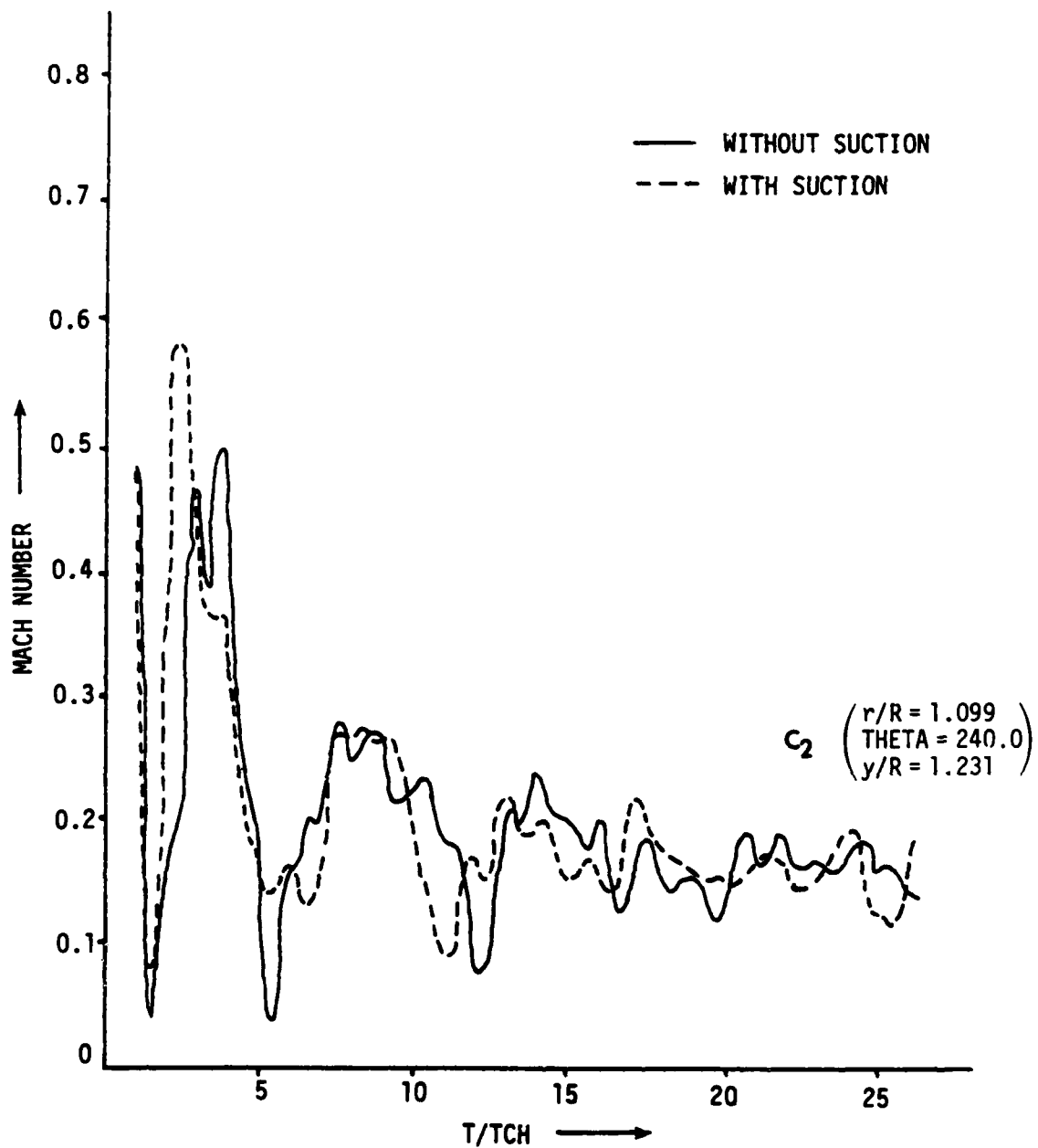


Figure 19. Local Mach Number Variation at Mesh Point C_2 .

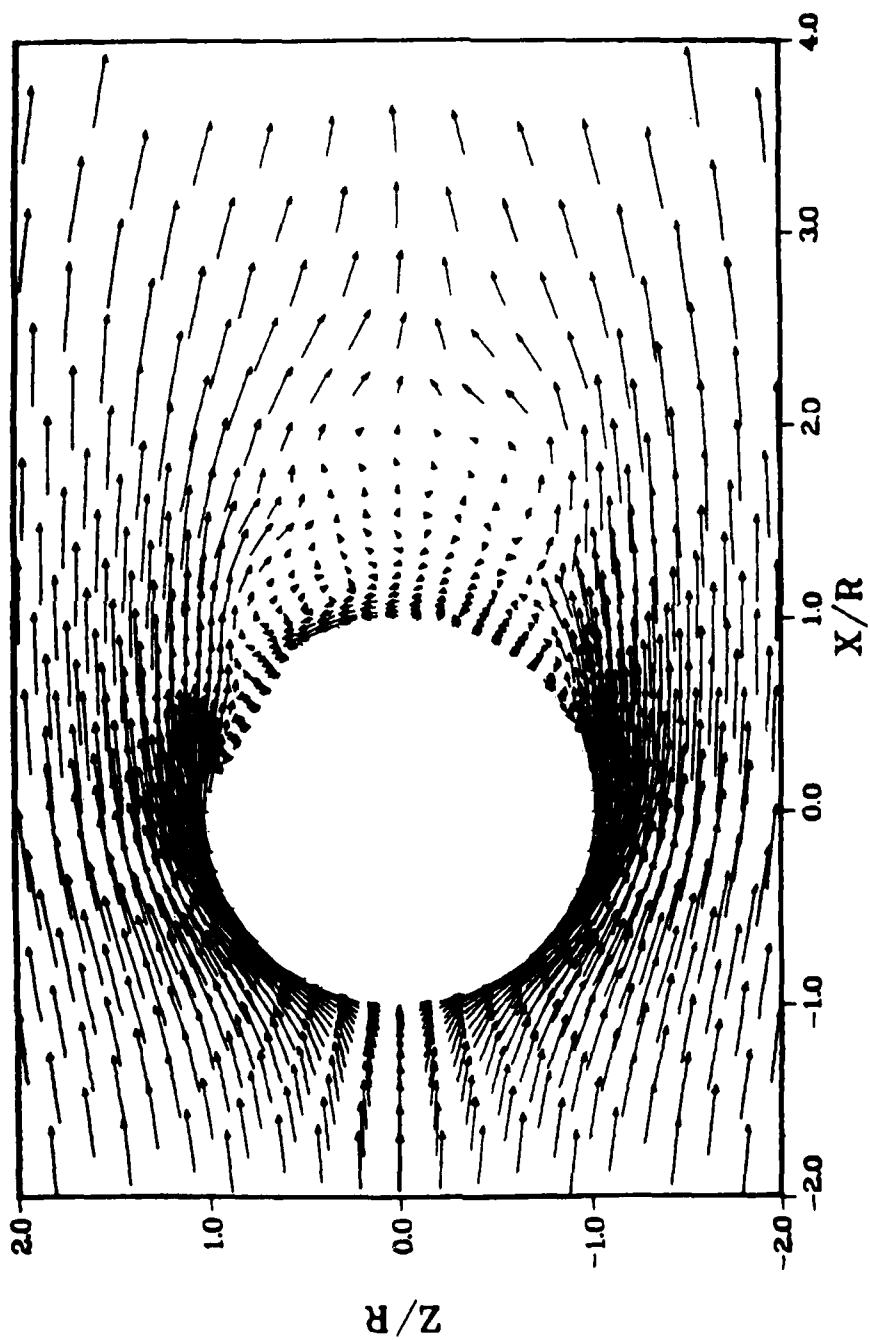


Figure 20. Instantaneous Velocity Field for Flow Without Suction in the Turret Shoulder Plane.

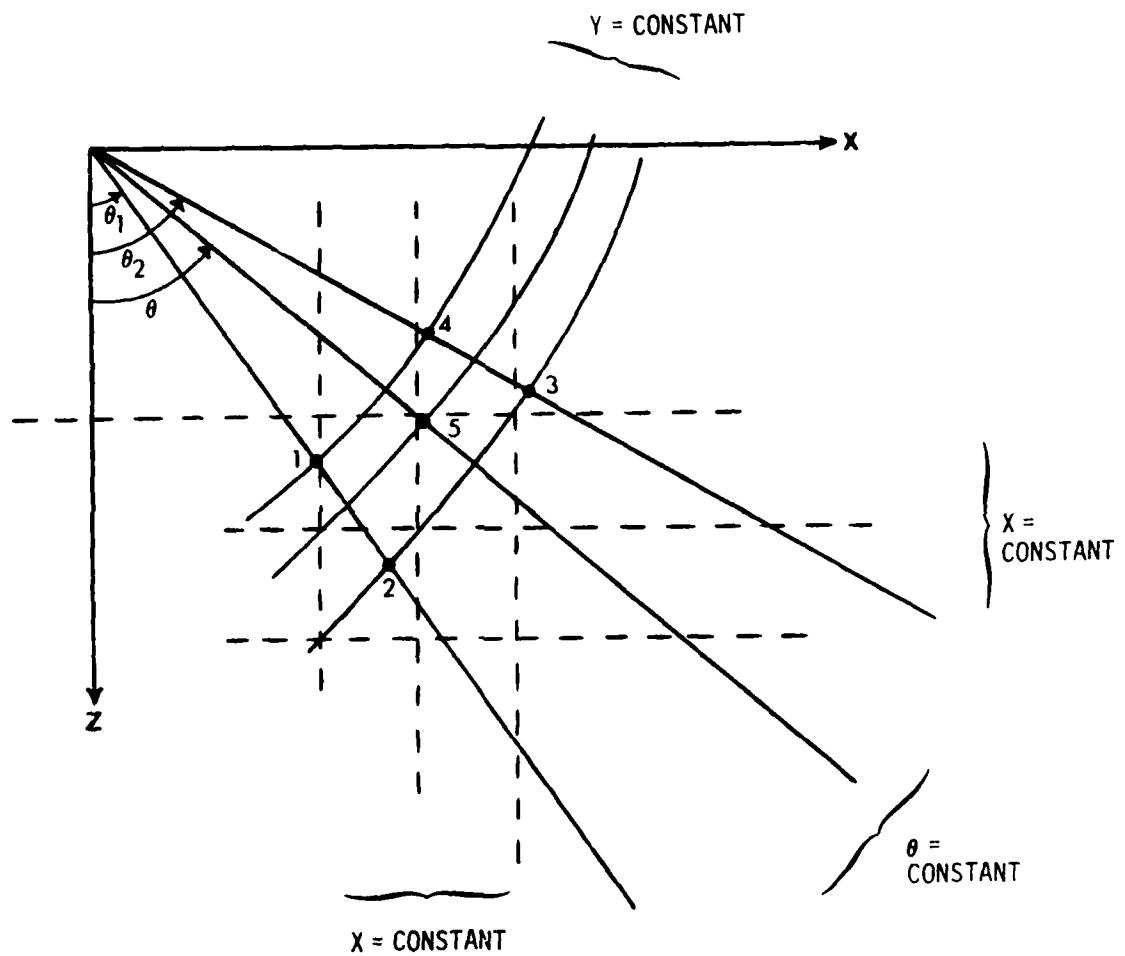


Figure 21. The Typical Mesh Points for Body-Oriented and Cartesian Coordinate System.

$$\begin{aligned}
 FP_5 = & \left(\frac{\gamma_5 - \gamma_1}{\gamma_2 - \gamma_1} \right) \left(\frac{\theta_5 - \theta_1}{\theta_3 - \theta_1} \right) \cdot FP_3 + \left(1 - \left(\frac{\gamma_5 - \gamma_1}{\gamma_2 - \gamma_1} \right) \left(\frac{\theta_5 - \theta_1}{\theta_3 - \theta_1} \right) \right) \cdot FP_4 \\
 & + \left(\frac{\gamma_5 - \gamma_1}{\gamma_2 - \gamma_1} \right) \left(1 - \frac{\theta_5 - \theta_1}{\theta_3 - \theta_1} \right) \cdot FP_2 + \left(1 - \frac{\gamma_5 - \gamma_1}{\gamma_2 - \gamma_1} \right) \left(1 - \frac{\theta_5 - \theta_1}{\theta_3 - \theta_1} \right) \cdot FP_1
 \end{aligned}
 \tag{47}$$

$\gamma_2 > \gamma_1, \theta_3 > \theta_1.$

It may be recalled that the point '5' is a Cartesian coordinate system point and such points can be selected along the line $x = \text{constant}$. The important aspect remaining is to identify the neighboring mesh points where the computation is performed. For the core without suction, the wake profiles and Mach number levels are presented in Figures 22 and 23, respectively.

When a uniform suction is applied, a striking contrast in the flowfield is observed, as presented in Figures 24 to 26. This is an excellent example of the three-dimensional flow interaction at the turret shoulder where the inflow from the top has sharply divided the wake into two parts. The local Mach number recorded in the vicinity of rear stagnation point was 0.6. At this location, the periodic mass exchange due to unsteady effect is evident but the characteristic flowfield remains similar. This behavior is very much in compliance with the earlier discussion regarding the pressure coefficient and Mach number.

Complementary to the turret shoulder plane is the cross-sectional plane ($0^\circ - 180^\circ$ azimuth angles) for which the instantaneous velocity field is presented in Figure 27. For the case when the turret is treated as a solid shell, the upstream influence is confined to the flat plate and is within one turret radius. In the downstream direction the wake region is extended up to three times the turret radius and is mainly affected by the separated flow from the turret top. The reverse flow and its

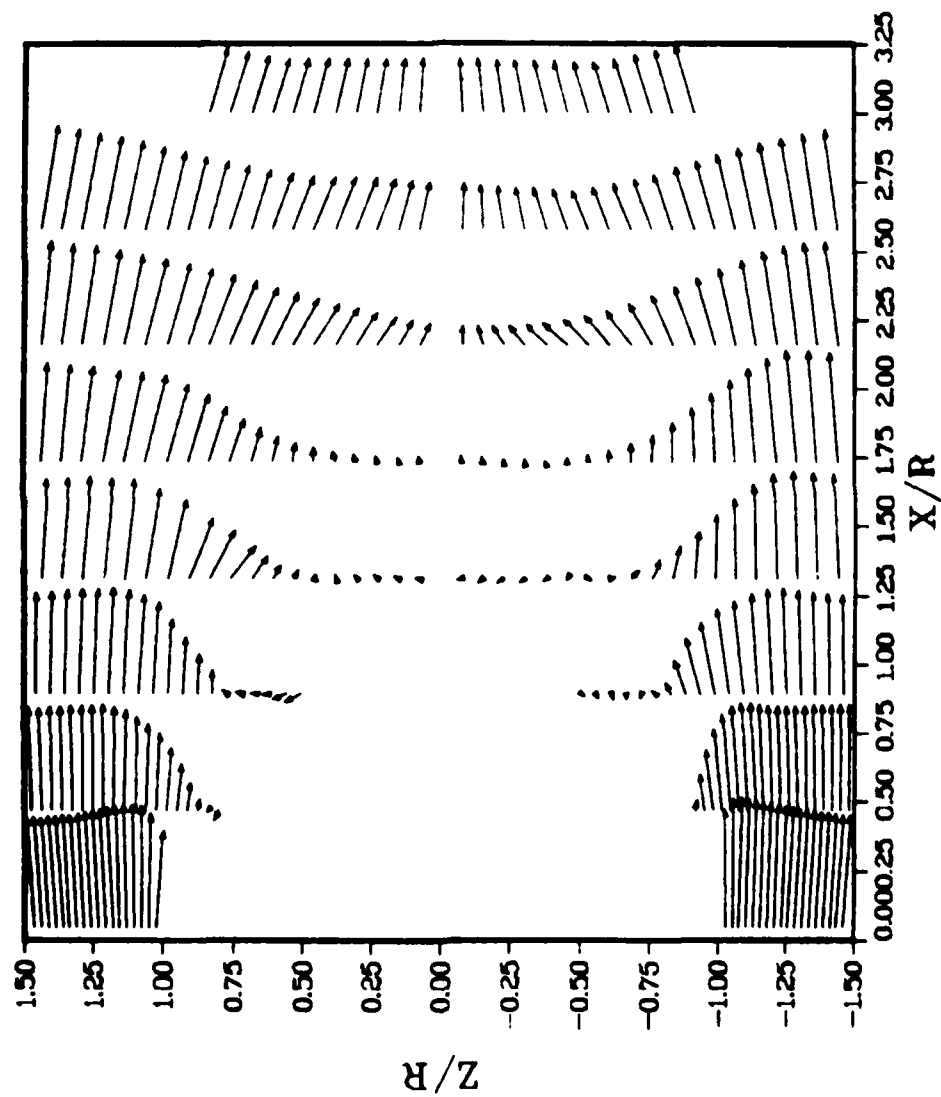


Figure 22. Wake Profiles for Flow Without Suction in the Turret Shoulder Plane.

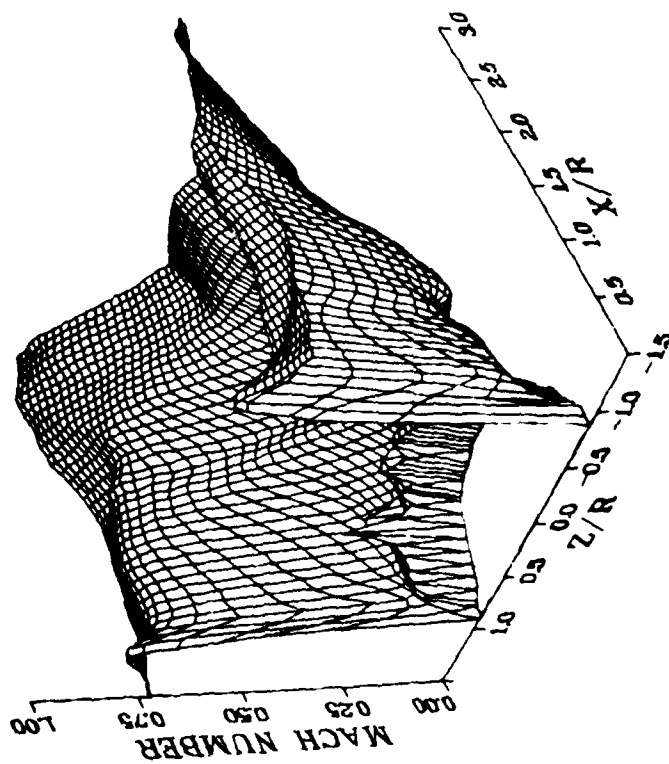


Figure 23. Planar Plot of the Mach Number Distribution for Flow Without Suction in the Target Shoulder Plane.

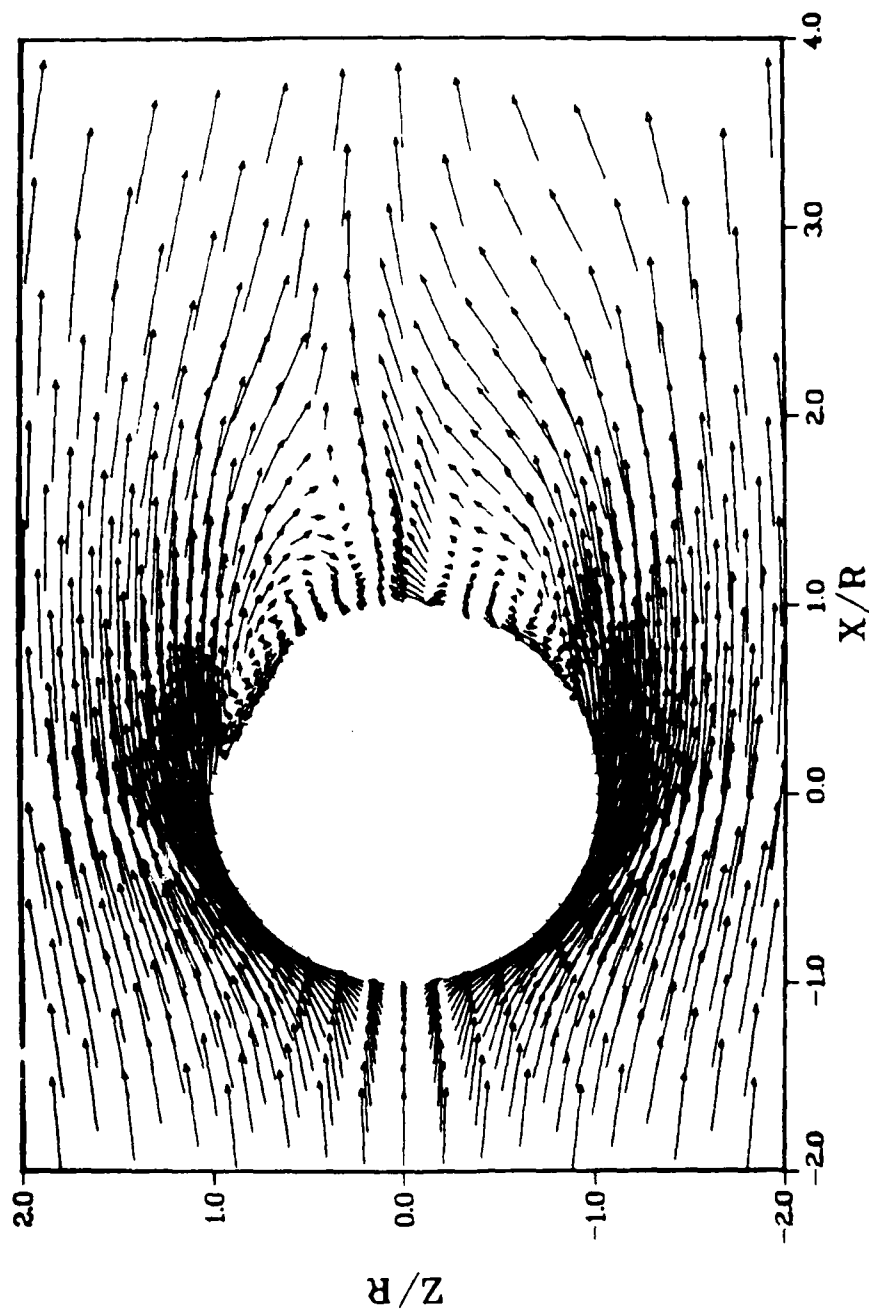


Figure 24. Instantaneous Velocity Field Flow with Suction in the Turret Shoulder Plane.

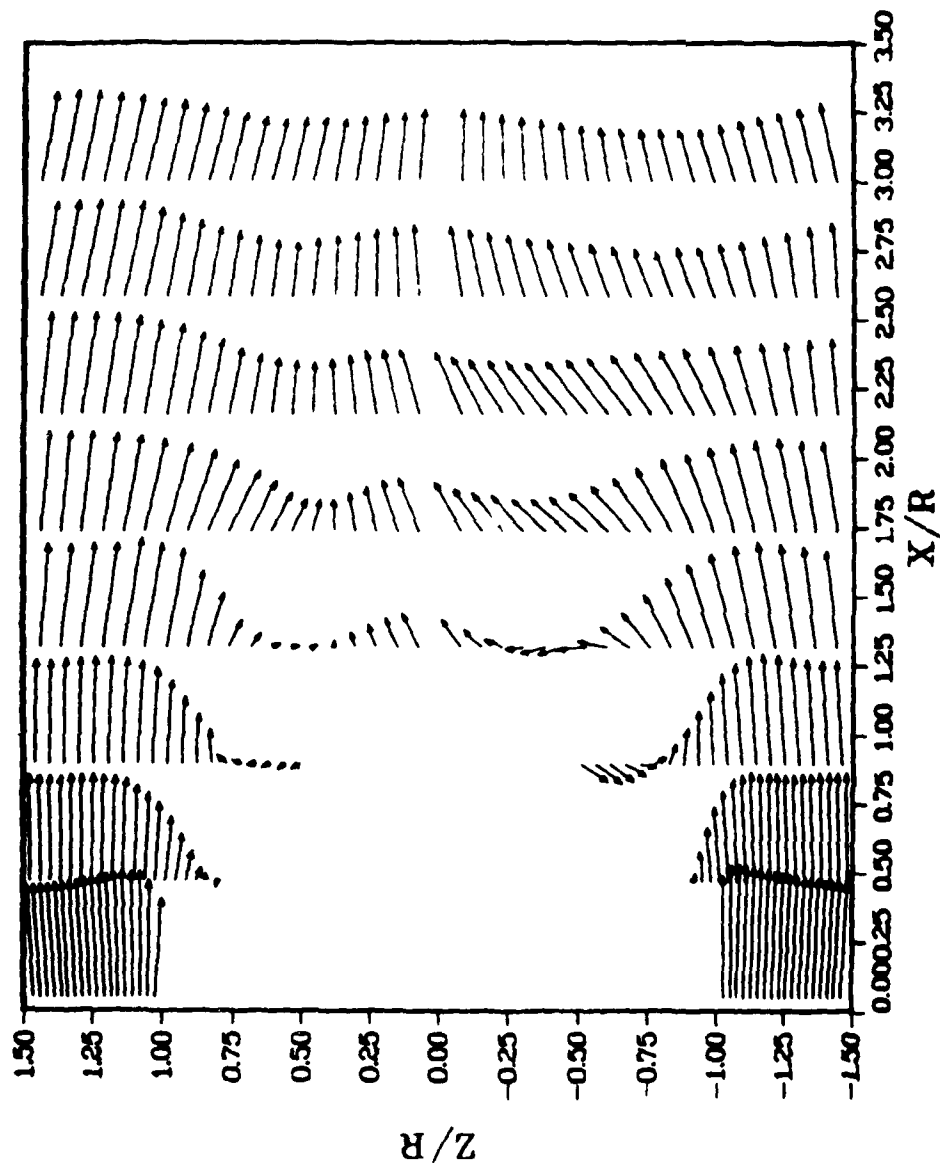


Figure 25. Wake profiles for Flow with Suction in the Turret Shoulder Plane.

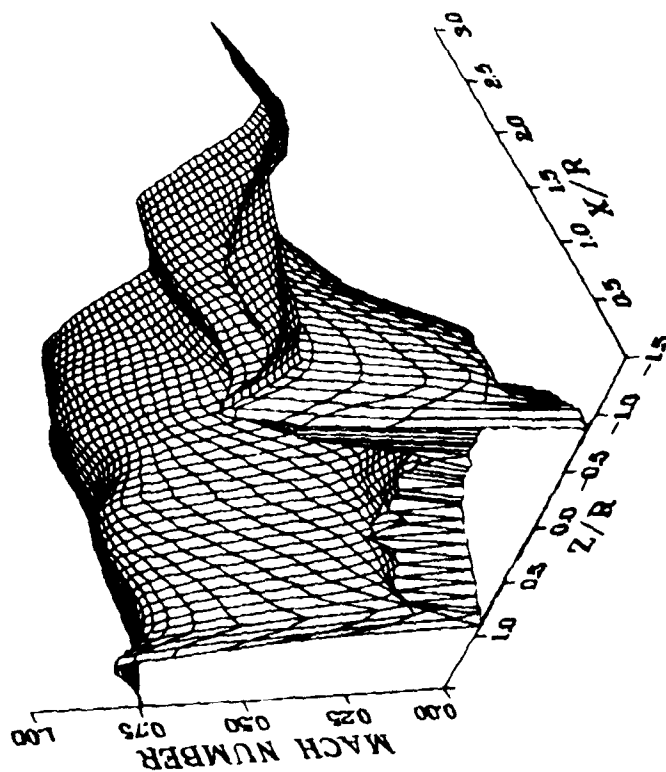


Figure 26. Planar plot of the Mach Number Distribution for flow with Suction in the Turret Shoulder.

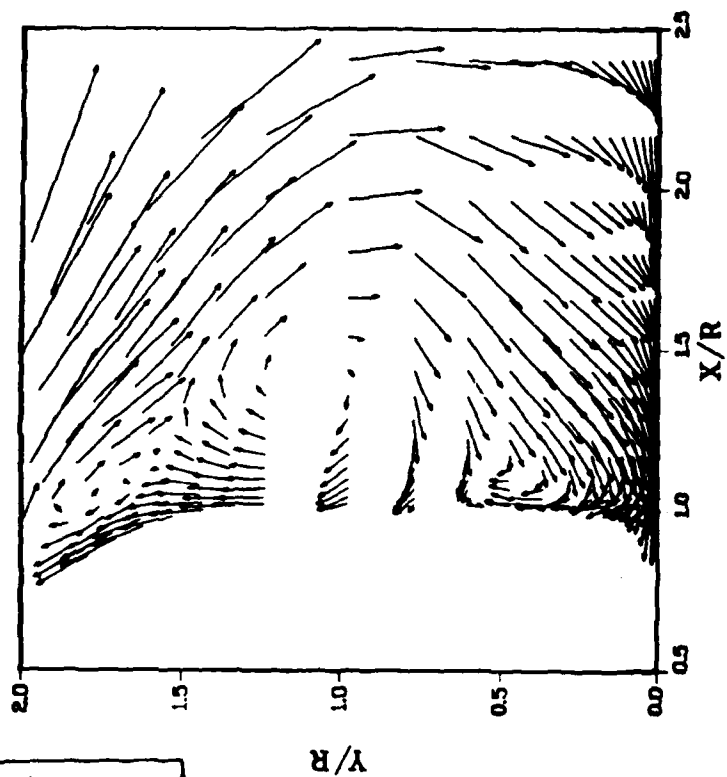
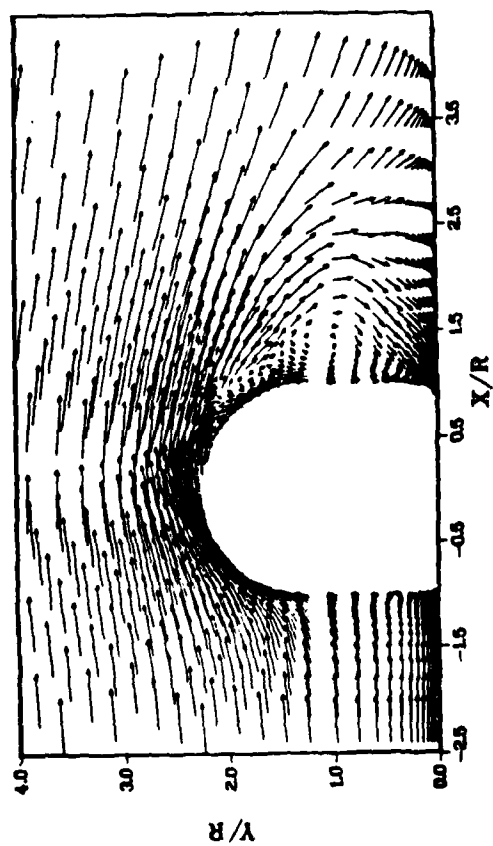
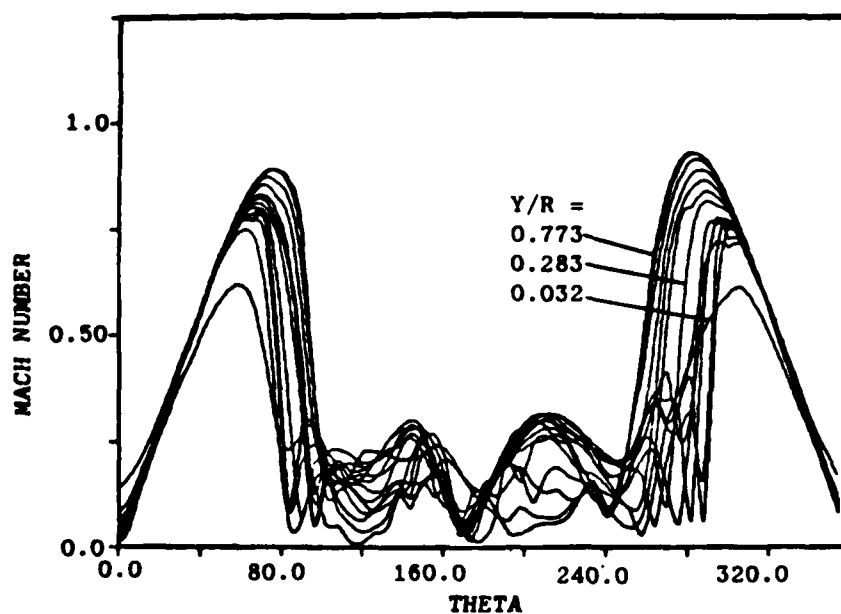


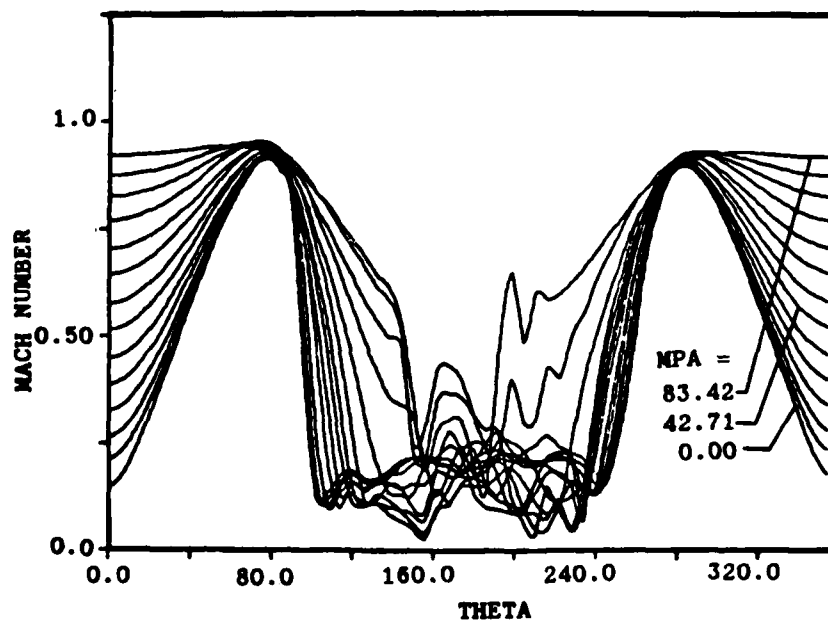
Figure 27. Velocity Field in the Cross-sectional plane for the Flow Without Suction.

time dependent variation provide the mechanism for vortex shedding and the relative movement of reattachment point. To estimate the three-dimensional Mach number distribution close to the hemispherical turret surface, we make use of the medium plane angle (MPA). The 0° MPA corresponds to the turret shoulder while 90° MPA corresponds to the turret top. Figure 28 gives one such instantaneous distribution for the same time level as that of the velocity field shown in Figure 27. It is interesting to observe that the maximum Mach number occurs at 89° AZA and 276° AZA and the minimum at the rear stagnation line neighborhood. This phenomena demonstrates a strong reverse flow on the turret surface and that the flow diverges from the stagnation line. A marked difference in these characteristics is observed in Figures 29 and 30 when the turret is considered to a porous shell. As a result of the small uniform suction, the separated and reverse flow regions are reduced substantially. In this case the flow at the turret top is attached and the maximum Mach number is located at 192° AZA. The local Mach number close to the surface crosses the sonic limit after 42° MPA.

A significant insight into the three-dimensional separated flow is offered by the limiting streamline pattern, which are, in the limiting case, the skin friction lines. These lines satisfy the topological criteria for the singular points. This confirmation was provided in our earlier work⁶ for the turret as well as for the flat plate surfaces. For this study also, the primary separation line and the horseshoe vortex structure for large protuberance (Figures 31 and 32) show an excellent agreement with the work of Sedney and Kitchens⁹. In Figures 33 and 34, we present two typical limiting streamline patterns (for one principal time period) on the turret surface. It can be observed that for the flow without suction, the turret top experiences a highly random flowfield behavior and the turbulence is prominent in the cutout side. This "opening" switches from cutout side to smooth side and back as the computation progresses. Thus, the separation line encounters an oscillatory phenomena beyond 60° MPA. This



(a) On the Cylinder



(b) On the Hemisphere

Figure 28. Mach Number Distribution Close to the Turret Surface for the Flow Without Suction.

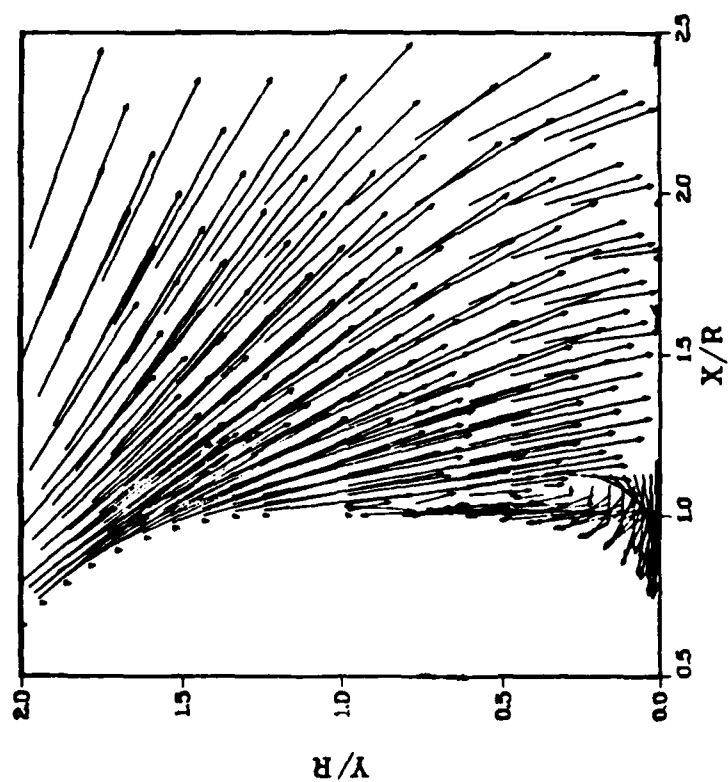
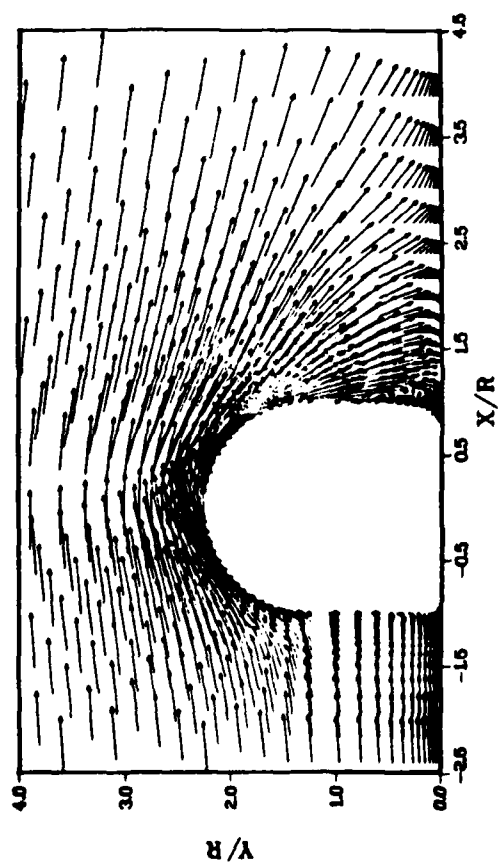
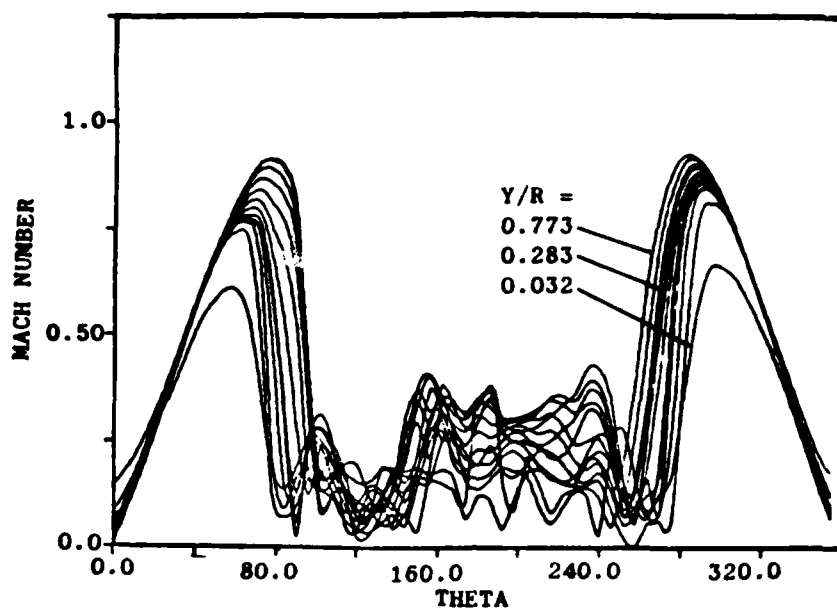
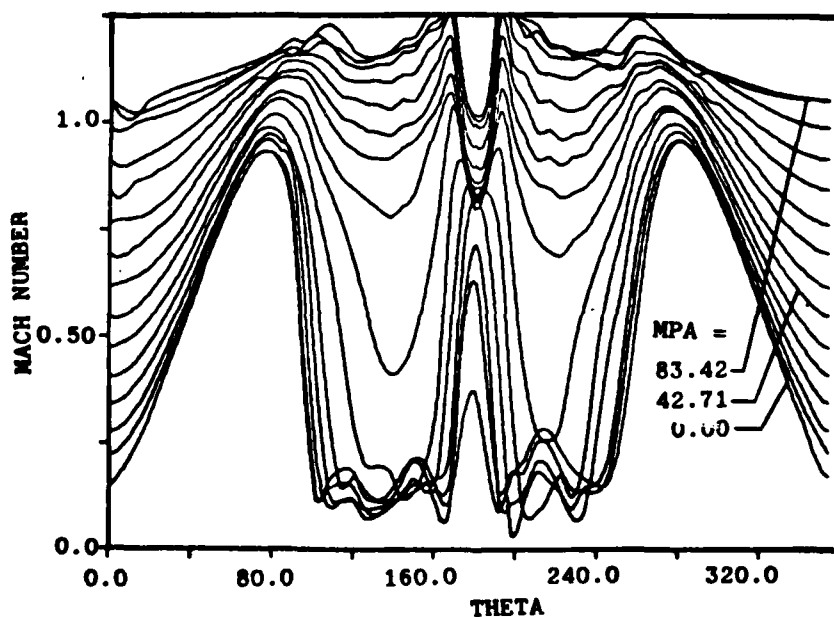


Figure 29. Velocity Field in the Cross-sectional Plane for the Flow With Suction.



(a) On the Cylinder



(b) On the Hemisphere

Figure 30. Mach Number Distribution Close to the Turret Surface for the Flow With Suction.

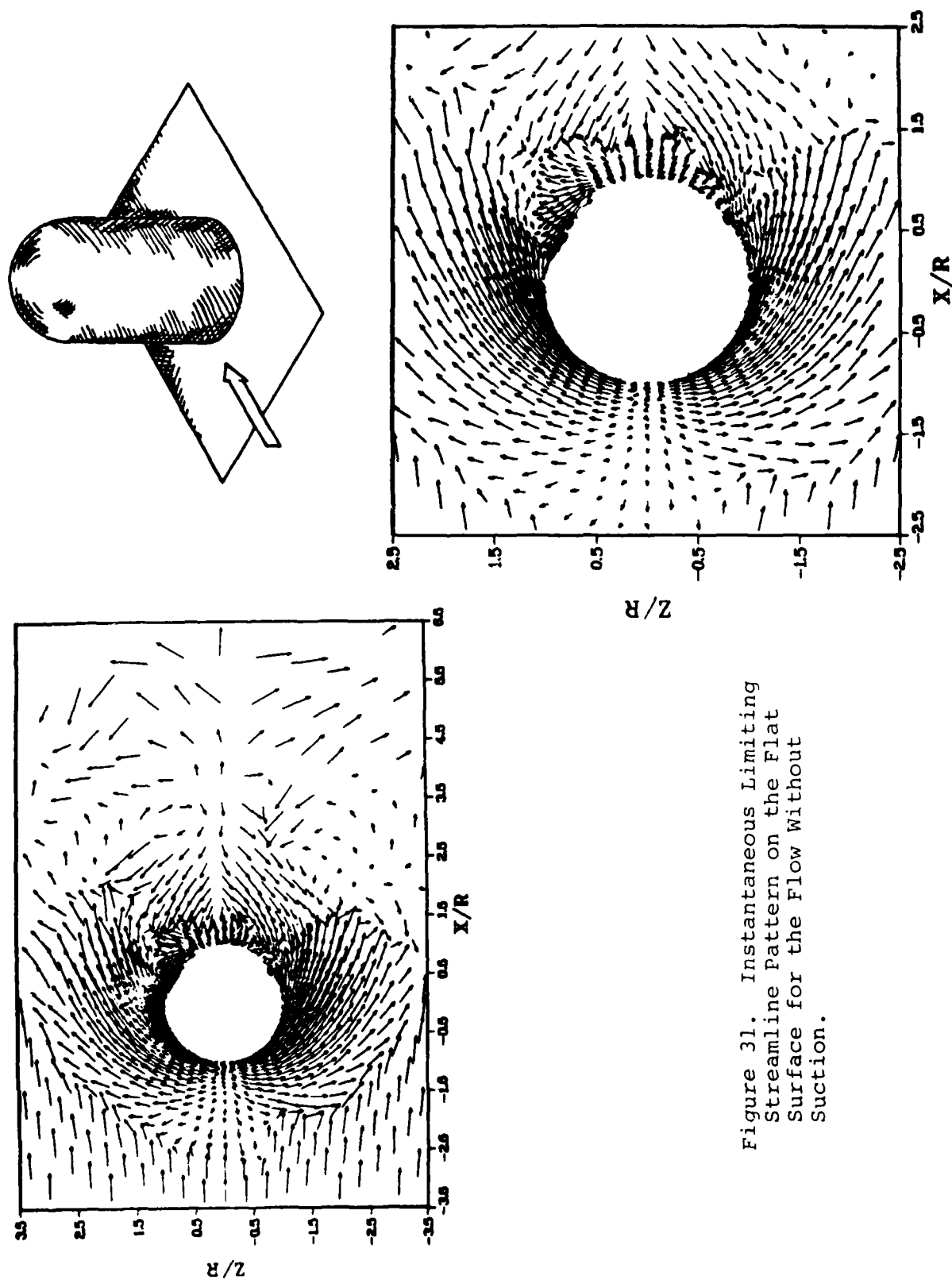


Figure 31. Instantaneous Limiting Streamline Pattern on the Flat Surface for the Flow Without Suction.

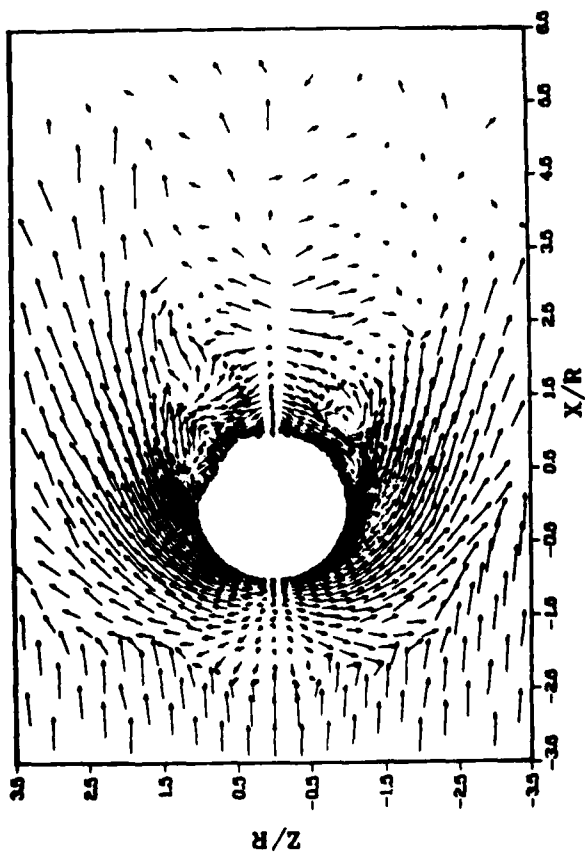
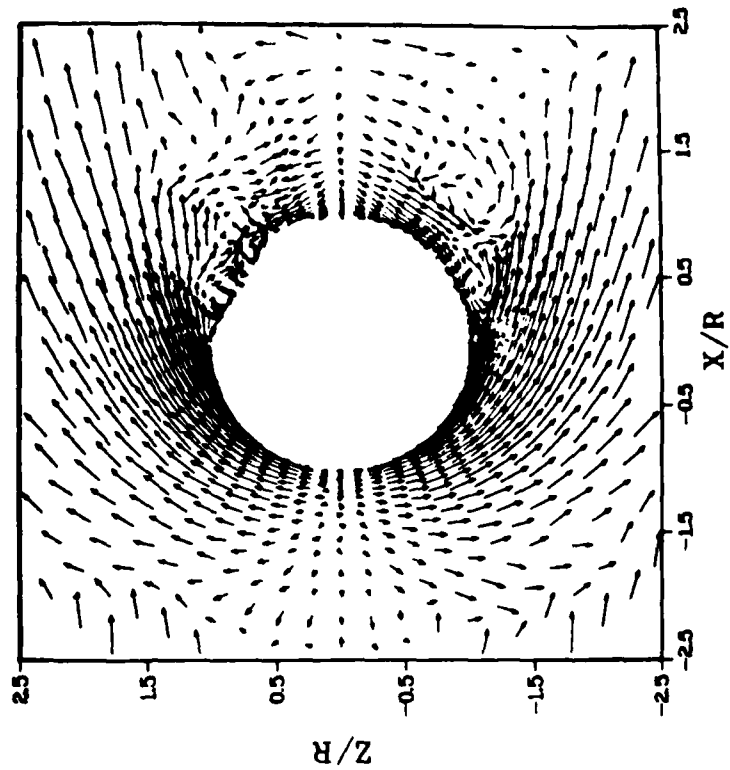
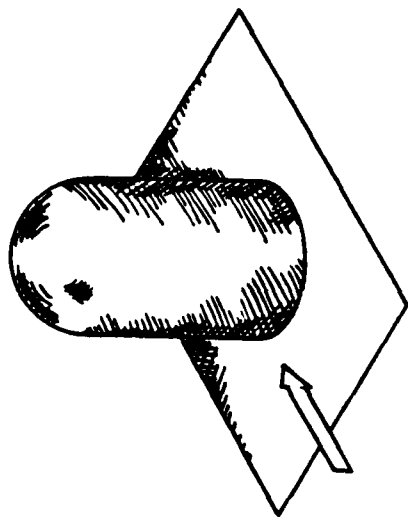


Figure 32. Instantaneous Limiting Streamline Pattern on the Flat Surface for the Flow with Suction.

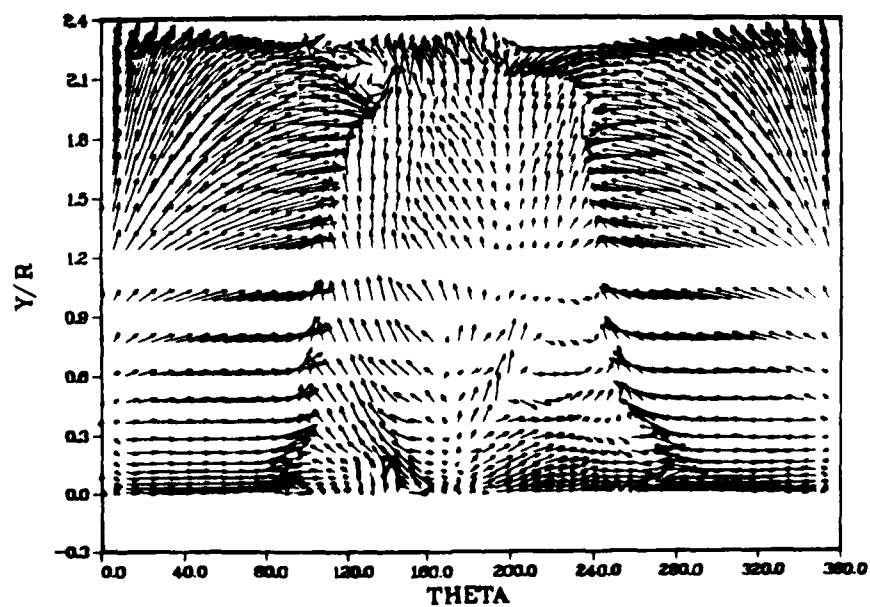
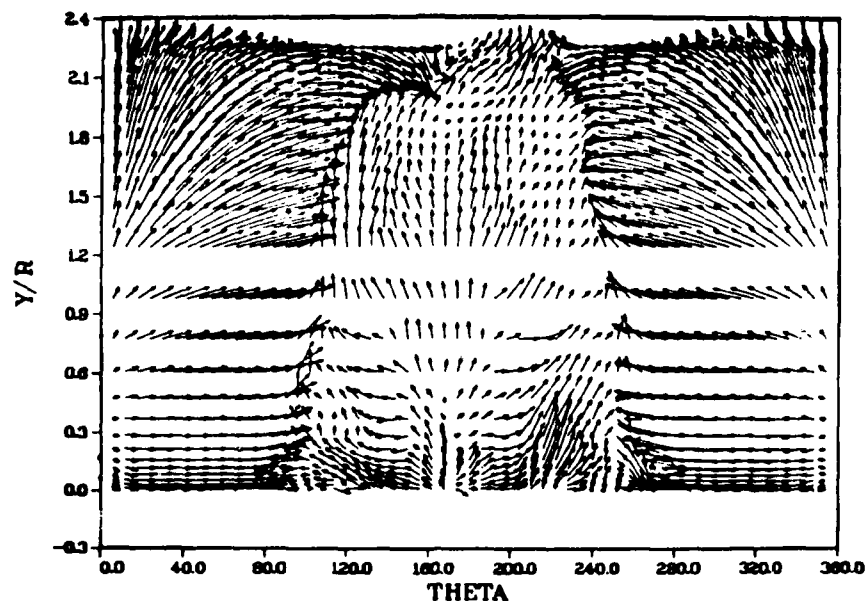


Figure 33. Instantaneous Limiting Streamline Pattern on the Turret Surface for Flow Without Suction.

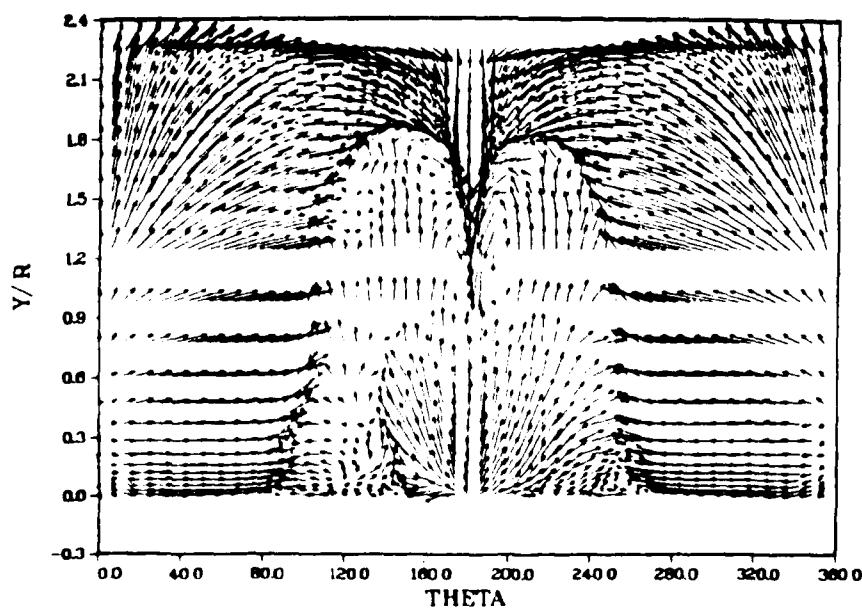
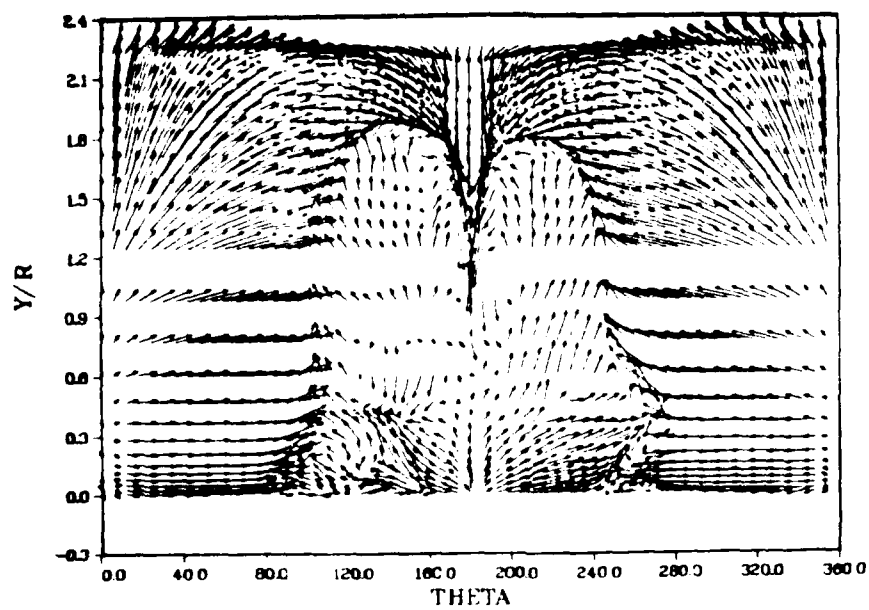


Figure 34. Instantaneous Limiting Streamline Pattern on the Turret Surface for Flow With Suction.

undesirable process is completely eliminated for the flow with uniform suction where the limiting streamline pattern exhibits a well organized motion. The disturbances caused by the turret cutout are only local and they do not affect the separation line location, in general.

In order to describe the oscillatory flowfield structure along 120° AZA at the turret shoulder, the statistical properties of unsteady density are analyzed. For compressible turbulent flow, the time mean and root-mean-square (RMS) values were calculated as

$$\bar{\rho} = \frac{1}{T_p} \int_t^{t+T_p} \rho_j \cdot dt \quad j = 1, 2, \dots, 30 \quad (48)$$

$$\langle \rho'^2 \rangle = \left[\frac{1}{T_p} \int_t^{t+T_p} \rho_j^2 \cdot dt - \left\{ \frac{1}{T_p} \int_t^{t+T_p} \rho_j \cdot dt \right\}^2 \right]^{1/2} \quad (49)$$

where $T_p = 0.0056$ second is equal to two principal time periods and is a function of Strouhal number, turret diameter and the free stream velocity. Since the time increment for the present analysis is very small, the straightforward integral procedure (48) and (49) were adopted. The density values, ρ_j at grid point location j , were recorded for 3400 consecutive time iterations ($CFL = 0.8$) and were integrated for both cases. The results are shown in terms of mean density, Figure 35, and $\langle \rho' \rangle / \langle \rho' \rangle_{\max} \%$, Figure 36, as functions of distance $\Delta R/R$ from the turret. The mean density near the turret surface reduces when suction is applied, indicating rapid expansion, but recovers its free stream value within one turret radius. It was also observed that during the time period, T_p , the difference in the mean fluctuation values of density between the flow without and with suction case were negligible. However, the RMS density fluctuations are higher for flow with suction. This was true for experimental as well as computational

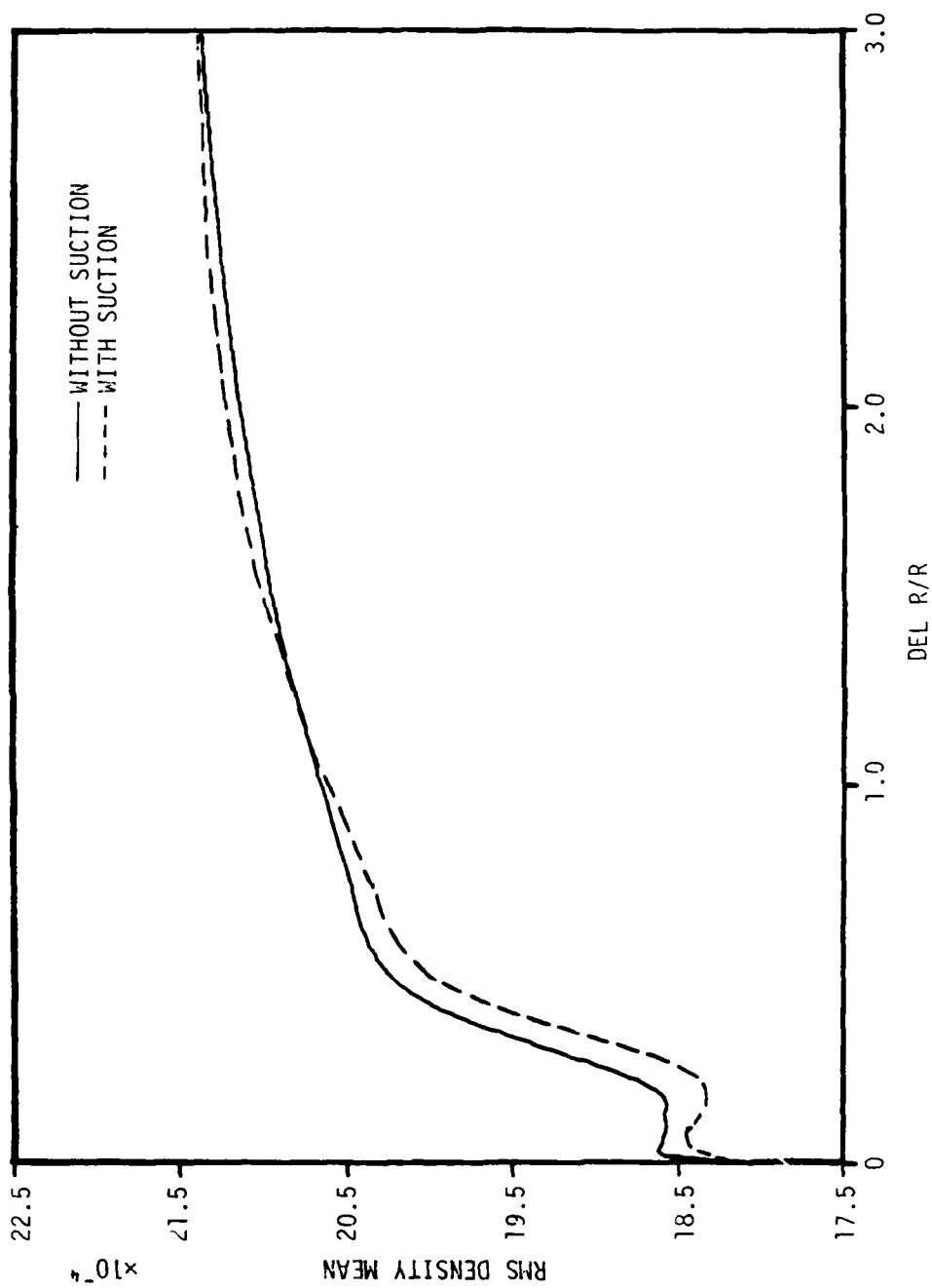


Figure 35. Mean Density Along 120° AZA.

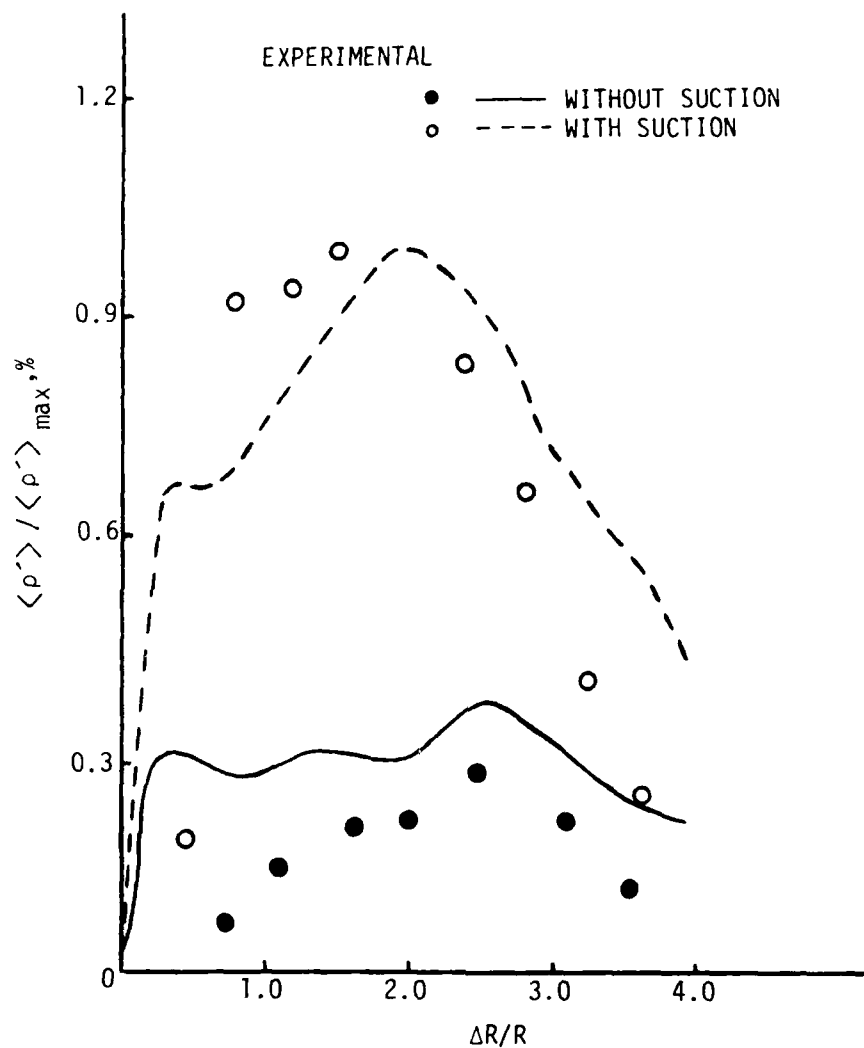


Figure 36. Comparison of RMS Density Fluctuations with Experimental Data.

values predicting a thinner shear layer. By virtue of clustering the mesh points near the turret surface, there seems to be a precise computational information in terms of density data. In this region, we did not have any experimental value to compare with. Away from the turret, even though the functional variation is similar, the computed results underpredict the density shear layer. For the experimental data, the ratio of the two peak RMS density values was 3.6780, while for computed results it is 2.850. This discrepancy can be partially attributed to the difference in the test and simulation conditions and the possible excessive vibration of the model during the test procedure¹. The computed results also can be improved by reducing grid space and introducing more mesh points. This might tax severely the available CRAY-1 memory and the computer resources. It was not possible at the present time, but a rigorous study in the three-dimensional mesh generation area is one of our future goals.

Continuing our analysis, the correlation coefficient, R_{mn} , for the density data at mesh point location j_m and j_n was evaluated as

$$R_{mn} = \frac{\frac{1}{T_p} \int_t^{t+T_F} (\rho_{j_m} - \bar{\rho}_{j_m}) \cdot (\rho_{j_n} - \bar{\rho}_{j_n}) \cdot dt}{\langle \rho_{j_m}^2 \rangle \cdot \langle \rho_{j_n}^2 \rangle} \quad (50)$$

$m, n = 1, 2, \dots, 30$

Evidently, R_{mn} is bounded and $R_{mm} = 1.0$ indicating that the density values at the mesh point location j_m are correlated. We have plotted, in Figures 37 and 38, the correlation coefficients for the first six mesh locations to emphasize the near field structure. During the time T_p , for the flow without suction, the function R_{mn} does not show any correlation and the shear layer is highly unstable. The uniform suction provides a coherence in the fluid flow behavior and a specific definition of shear layer width. Beyond the shear layer, the numerical value of R_{mn} oscillates close to zero.

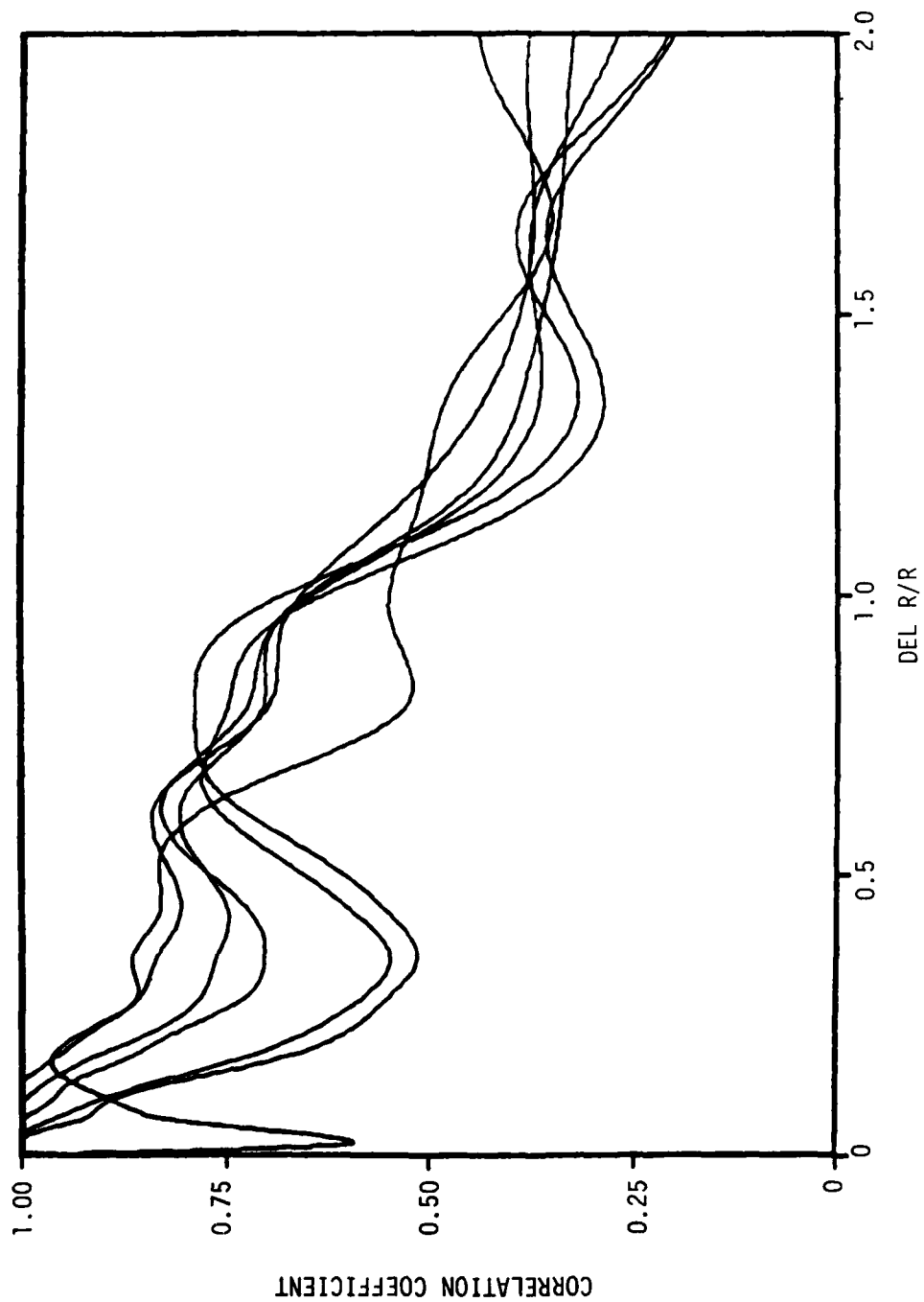


Figure 37. Correlation Coefficient for Flow Without Suction.

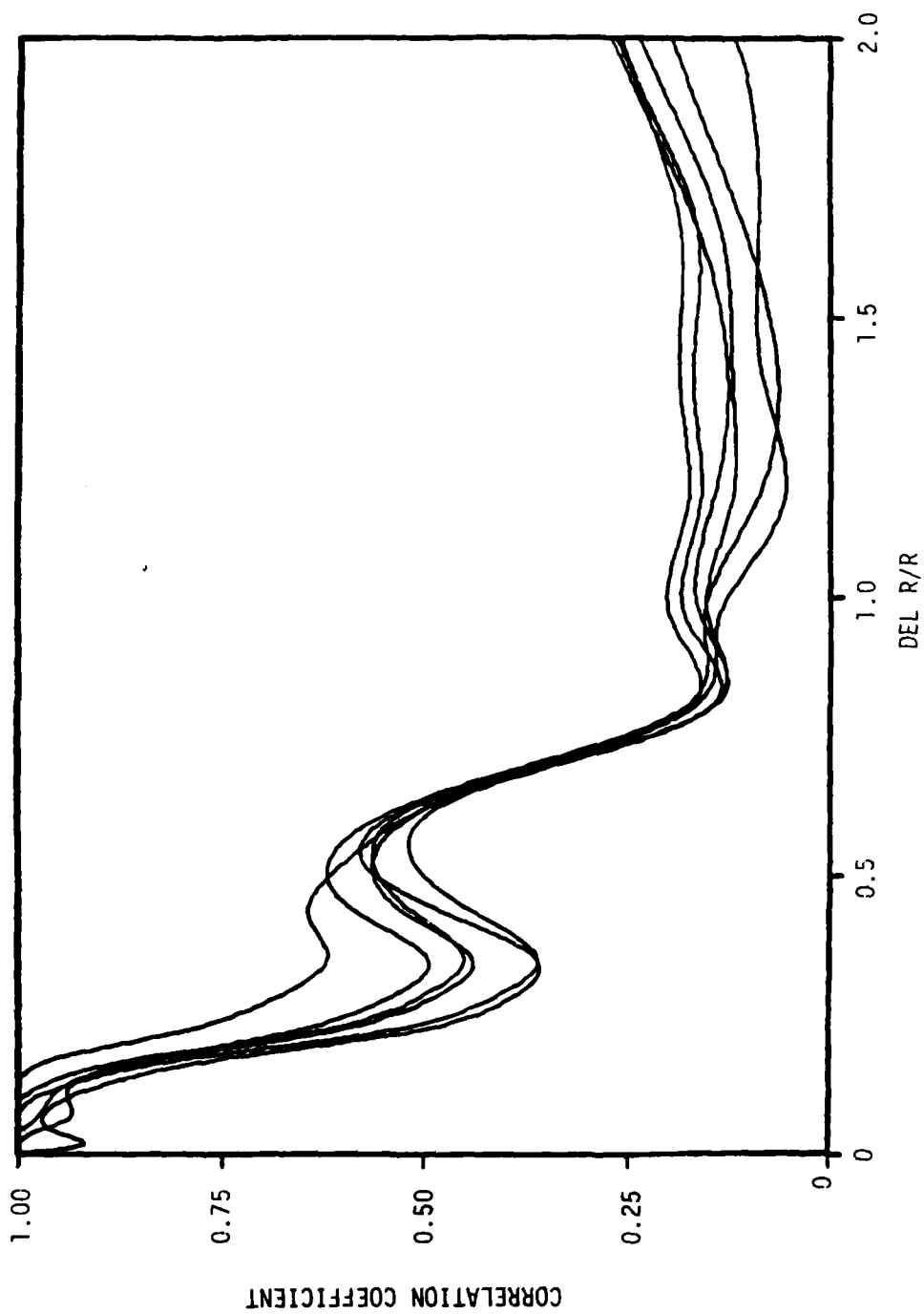


Figure 38. Correlation Coefficient for Flow With Suction.

Finally, along 120° AZA, a spectral analysis is done for all possible modes of oscillations. Such evaluation is one of the important aspects of unsteady fluid dynamics. We accomplish this goal through the ninety term Fourier series. The computation is done for all the grid points and Figure 39 is the representative graph for the location $\Delta R/R = 0.486$. The first peak is observed at the frequency 349.83 Hz which corresponds to the Strouhal number²⁵ 0.2265. The higher modes of the spectral analysis exhibit a complete random behavior; no single discrete frequency is dominated over the other. Based on the phase angle analysis (Figure 40), we conclude that the highest credible frequency range of our numerical analysis is around 6.4 KHz. This limitation can only be eliminated by using a much finer mesh point system.

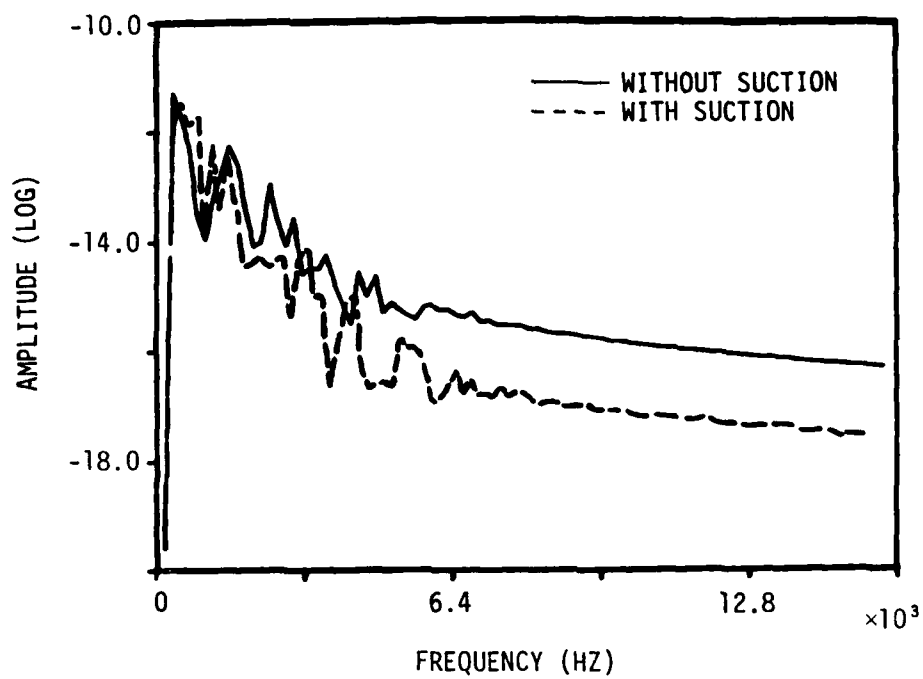
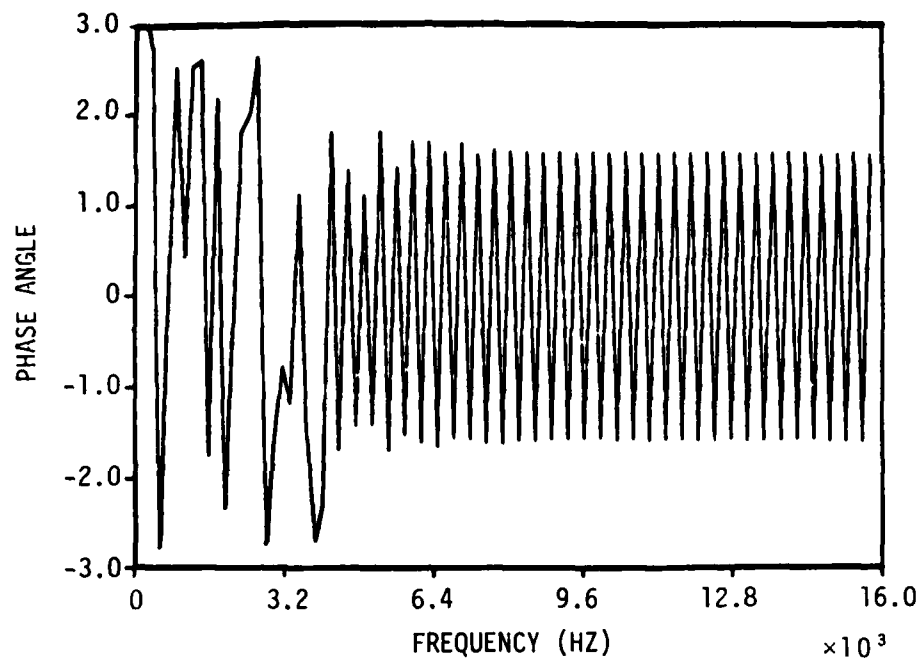
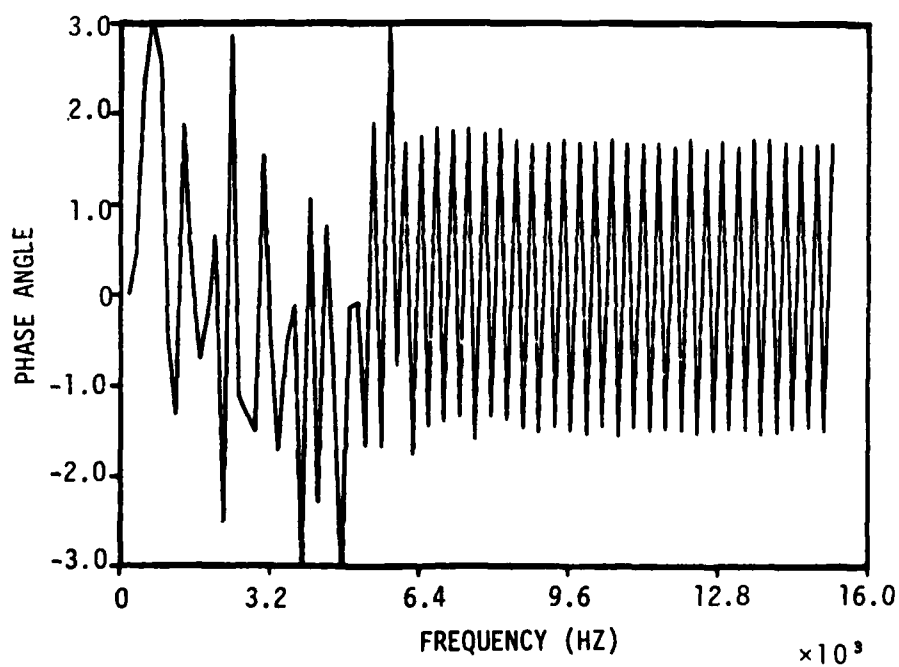


Figure 39. Spectral Analysis Along 120° AZA.



(a) Without Suction



(b) With Suction

Figure 40. Phase Angle Analysis Along 120° AZA.

SECTION 6

CONCLUSIONS

For a Mach number of 0.6 and Reynolds number of $12.8 \times 10^6/m$, the numerical simulation of time dependent three-dimensional separated flow is accomplished. It is established that a uniform suction at the turret surface causes a significant variation in the wake structure. Qualitative agreement is obtained for the general flowfield including RMS density fluctuation and correlation coefficient. However, in order to achieve better resolution, the optimum rearrangement of grid points in all three directions should continue to be stressed in future investigations.

APPENDIX - VORTICITY FUNCTION

The vorticity in the three-dimensional space is given by

$$\vec{\omega} = \nabla \times \vec{u} \quad (A-1)$$

$$= \begin{vmatrix} \hat{n}_1 & \hat{n}_2 & \hat{n}_3 \\ \frac{\partial}{\partial x} & \frac{\partial}{\partial y} & \frac{\partial}{\partial z} \\ u & v & w \end{vmatrix}$$

$$= \hat{n}_1 \left(\frac{\partial w}{\partial y} - \frac{\partial v}{\partial z} \right) + \hat{n}_2 \left(\frac{\partial u}{\partial z} - \frac{\partial w}{\partial x} \right) + \hat{n}_3 \left(\frac{\partial v}{\partial x} - \frac{\partial u}{\partial y} \right) \quad (A-2)$$

where \hat{n}_1 , \hat{n}_2 , \hat{n}_3 are the unit vectors in x, y, and z directions, respectively. The magnitude of this vorticity vector is, then, given by

$$|\vec{\omega}| = \frac{1}{2} \cdot \sqrt{\vec{\omega} \cdot \vec{\omega}} = \frac{1}{2} \left\{ \left(\frac{\partial w}{\partial y} - \frac{\partial v}{\partial z} \right)^2 + \left(\frac{\partial u}{\partial z} - \frac{\partial w}{\partial x} \right)^2 + \left(\frac{\partial v}{\partial x} - \frac{\partial u}{\partial y} \right)^2 \right\}^{0.5} \quad (A-3)$$

To evaluate the magnitude of vorticity in the body oriented coordinate system ξ , η , ζ , we use the Jacobian of transformation, J_n , to give

$$\begin{aligned} |\vec{\omega}| = 0.5 \left[\left\{ \left(\frac{\partial \xi}{\partial y} \cdot \frac{\partial w}{\partial \xi} + \frac{\partial \eta}{\partial y} \cdot \frac{\partial w}{\partial \eta} + \frac{\partial \zeta}{\partial y} \cdot \frac{\partial w}{\partial \zeta} \right) \right. \right. \\ \left. \left. - \left(\frac{\partial \xi}{\partial z} \cdot \frac{\partial v}{\partial \xi} + \frac{\partial \eta}{\partial z} \cdot \frac{\partial v}{\partial \eta} + \frac{\partial \zeta}{\partial z} \cdot \frac{\partial v}{\partial \zeta} \right) \right\}^2 \right. \\ \left. + \left\{ \left(\frac{\partial \xi}{\partial z} \cdot \frac{\partial u}{\partial \xi} + \frac{\partial \eta}{\partial z} \cdot \frac{\partial u}{\partial \eta} + \frac{\partial \zeta}{\partial z} \cdot \frac{\partial u}{\partial \zeta} \right) \right. \right. \\ \left. \left. - \left(\frac{\partial \xi}{\partial x} \cdot \frac{\partial w}{\partial \xi} + \frac{\partial \eta}{\partial x} \cdot \frac{\partial w}{\partial \eta} + \frac{\partial \zeta}{\partial x} \cdot \frac{\partial w}{\partial \zeta} \right) \right\}^2 \right. \\ \left. + \left\{ \left(\frac{\partial \xi}{\partial x} \cdot \frac{\partial v}{\partial \xi} + \frac{\partial \eta}{\partial x} \cdot \frac{\partial v}{\partial \eta} + \frac{\partial \zeta}{\partial x} \cdot \frac{\partial v}{\partial \zeta} \right) \right. \right. \\ \left. \left. - \left(\frac{\partial \xi}{\partial y} \cdot \frac{\partial u}{\partial \xi} + \frac{\partial \eta}{\partial y} \cdot \frac{\partial u}{\partial \eta} + \frac{\partial \zeta}{\partial y} \cdot \frac{\partial u}{\partial \zeta} \right) \right\}^2 \right]^{0.5} \quad (A-4) \end{aligned}$$

On the turret surface, the derivatives in the ξ -direction and ζ -direction vanish. Thus, the surface vorticity, ω_w , can be expressed as

$$|\vec{\omega}_w| = 0.5 \left[\left(\frac{\partial \eta}{\partial y} \cdot \frac{\partial w}{\partial \eta} - \frac{\partial \eta}{\partial z} \cdot \frac{\partial v}{\partial \eta} \right)^2 + \left(\frac{\partial \eta}{\partial z} \cdot \frac{\partial u}{\partial \eta} - \frac{\partial \eta}{\partial x} \cdot \frac{\partial w}{\partial \eta} \right)^2 + \left(\frac{\partial \eta}{\partial x} \cdot \frac{\partial v}{\partial \eta} - \frac{\partial \eta}{\partial y} \cdot \frac{\partial u}{\partial \eta} \right)^2 \right]^{0.5} \quad (\text{A-5})$$

REFERENCES

1. Gilbert, K. G. and Otten, L. G. (Ed.), "Aero-optical Phenomena," Progress in Aeronautics and Astronautics, Vol. 80, 1982.
2. DeJonckheere, R. K., Russell, J. J. and Chou, D. C., "High Subsonic Flow Field Measurements and Turbulent Flow Analysis Around a Turret Protuberance," AIAA Paper No. 82-0057, AIAA 20th Aerospace Sciences Meeting, January 11-14, 1982, Orlando, Florida.
3. Haslund, R. L., Small Scale Flow Control Investigation, AFWL-TR-82-69, November 1982.
4. Rose, W. L., The Effect of Flow Control on Optical Propagation Characteristics on a Small Scale Turret Model, AFWL-ARL-TN-82-003, March 1982.
5. DeJonckheere, R. K. and Chou, D. C., "Experimental and Analytical Scaling on the Flow Field Around a Protuberance of High Subsonic Speed," AIAA Paper No. 82-1371, AIAA 9th Atmospheric Flight Dynamics Conference, August 9-11, 1982, San Diego, California.
6. Purohit, S. C., Shang, J. S. and Hankey, W. L., "Numerical Simulation of Flow Around a Three-Dimensional Turret," AIAA Paper No. 82-1020, AIAA/ASME 3rd Joint Thermophysics, Fluid, Plasma, and Heat Transfer Conference, St. Louis, Missouri, June 7-11, 1982.
7. Peake, D. J. and Tobak, M. "Topology of Two-Dimensional and Three-Dimensional Separated Flows," AIAA Paper No. 79-1480, AIAA 12th Fluid and Plasma Dynamics Conference, Williamsburg, Virginia, July 23-25, 1979.
8. Hunt, J. C. R., Abell, C. J. and Peterka, J. A., "Kinematical Studies of the Flow Around Free or Surface Mounted Obstacle; Applying Topology to Flow Visualization," J. Fluid Mechanics, Vol. 86, pt. 1, 1978, pp. 179-200.
9. Sedney, R. and Kitchens, C. W., The Structure of Three-Dimensional Separated Flow in Obstacle Boundary Layer Interaction, AGARD-CP-168, 1975.
10. Chapman, D. R., "Dryden Lectureship in Research, Computational Aerodynamic Development and Outlook," AIAA Journal, Vol. 17, No. 12, December 1979, pp. 1293-1313.
11. Hollanders, H. and Viviand, H., "The Numerical Treatment of Compressible High Reynolds Number Flows," Computational Fluid Dynamics, Ed., W. Kollman, Hemisphere Publishing Corporation, 1981.

12. Thompson, J. F., Thames, F. C. and Mastin, C. W., Boundary-Fitted Curvilinear Co-ordinate System for Solution of Partial Differential Equations on Fields Containing Any Number of Arbitrary Two-Dimensional Bodies, NASA CR-2729, 1977.
13. Shang, J. S., "Numerical Simulation of Wing-Fuselage Interference," AIAA Paper No. 81-0048, AIAA 19th Aerospace Sciences Meeting, January 12-15, 1981, St. Louis, Missouri.
14. Reyhner, T. A., A Computer Program for Finite Difference Calculation of Compressible Turbulent Boundary Layers, Boeing Document D6-23236, Boeing Commercial Airplane Company, Seattle, Washington, 1970.
15. Syberg, J. and Koncsek, J. L., "Bleed System Design Technology for Supersonic Inlets," Journal of Aircraft, Vol. 10, No. 7, July 1973.
16. Baldwin, B. S. and Lomax, H., "Thin Layer Approximation and Algebraic Model for Separated Turbulent Flows," AIAA Paper No. 78-257, AIAA 16th Aerospace Sciences Meeting, Huntsville, Alabama, January 16-18, 1978.
17. Shang, J. S., Smith, R. E. and Hankey, W. L., "Flow Oscillation of Spike-Tipped Bodies," AIAA Paper No. 80-0062, AIAA 18th Aerospace Sciences Meeting, Pasadena, California, January 14-16, 1980.
18. Knight, D. D., "A Hybrid Explicit-Implicit Numerical Algorithm for the Three-Dimensional Compressible Navier-Stokes Equations," AIAA Paper No. 83-0223, AIAA 21st Aerospace Sciences Meeting, January 10-13, 1983, Reno, Nevada.
19. Knight, D. D., private communication, 1982.
20. Shang, J. S., Bunning, P. G., Hankey, W. L. and Writh, M. C., "Performance of a Vectorized Three-Dimensional Navier-Stokes Code on a CRAY-1 Computer," AIAA Journal, Vol. 18, No. 9, September 1980, pp. 1073-1079.
21. McCormack, R. W., "The Effect of Viscosity in Hypersonic Impact Cratering," AIAA Paper No. 69-354, 1969.
22. McCormack, R. W., "Numerical Solution of the Interaction of Shock Wave with a Laminar Boundary Layer," Lecture Notes in Physics, Vol. 8, Springer-Verlag, 1971, pp. 151-163.
23. Cebeci, T., "Calculation of Compressible Turbulent Boundary Layers with Heat and Mass Transfer," AIAA Paper No. 70-741, AIAA 3rd Fluid and Plasma Dynamics Conference, Los Angeles, California, June 29-July 1, 1970.

24. Shang, J. S., "Oscillatory Compressible Flow Around a Cylinder," AIAA Paper No. 82-0098, AIAA 20th Aerospace Sciences Meeting, January 11-14, 1982, Orlando, Florida.
25. Schlichting, H., Boundary Layer Theory, McGraw Hill, New York, 6th edition, 1968.

**DA
FILM**